International Journal of Pressure Vessels and Piping 120-121 (2014) 1–18

Contents lists available at ScienceDirect

International Journal of Pressure Vessels and Piping

journal homepage: www.elsevier.com/locate/ijpvp

A numerical investigation of constraint effects in circumferentially cracked pipes and fracture specimens including ductile tearing

Diego F.B. Sarzosa, Claudio Ruggieri*

Department of Naval Architecture and Ocean Engineering, University of São Paulo, São Paulo SP 05508–900, Brazil

ARTICLE INFO

Article history:
Received 23 October 2013
Received in revised form
9 March 2014
Accepted 26 March 2014
Available online 4 April 2014

Keywords:
Constraint
J–*Q* approach
Ductile tearing
Fracture specimens
Circumferentially cracked pipes

ABSTRACT

This work addresses a two-parameter description of crack-tip fields in bend and tensile fracture specimens incorporating the evolution of near-tip stresses following stable crack growth with increased values of the crack driving force as characterized by *J*. The primary objective of this study is twofold. First, the present investigation broadens current understanding on the role of constraint and test conditions in defect assessment procedures for pipeline girth welds using SE(T) and SE(B) specimens. Second, the work addresses the potential coupled effects of geometry and ductile tearing on crack-tip constraint as characterized by the *J*–*Q* theory which enables more accurate correlations of crack growth resistance behavior in conventional fracture specimens. Plane-strain and 3-D finite element computations including stationary and growth analyses are conducted for 3P SE(B) and clamped SE(T) specimens having different notch depth (a) to specimen width (W) ratio in the range $0.1 \leq a/W \leq 0.5$. Additional 3-D finite element analyses are also performed for circumferentially cracked pipes with a surface flaw having different crack depth (a) over pipe wall thickness (t) ratios and fixed crack length. A computational cell methodology to model Mode I crack extension in ductile materials is utilized to describe the evolution of *J* with the accompanying evolving near-tip opening stresses. Laboratory testing of an API 5L X70 steel at room temperature using standard, deeply cracked C(T) specimens is used to measure the crack growth resistance curve for the material and to calibrate the key cell parameter defined by the initial void fraction, f_0. A key result emerging from this study is that shallow crack SE(B) specimens can accurately and conservately produce crack growth resistance curves that describe well the measuring toughness capacity of circumferentially cracked pipes under remote bending. The present results provide additional understanding of the effects of constraint on crack growth which contributes to further evaluation of crack growth resistance properties in pipeline steels using SE(T) and SE(B) specimens while, at the same time, eliminating some restrictions against the use of shallow cracked bend specimens in defect assessment procedures.

1. Introduction

Substantial progress has been made in recent years in fitness-for-service (FFS) procedures applicable to defect assessments and life-extension programs of critical engineering structures. These methodologies, also referred to as Engineering Critical Assessment (ECA) procedures, provide a concise framework to correlate crack size with applied loading in terms of failure assessment diagrams (FAD) to evaluate the severity of crack-like flaws [1–3]. A key feature of these approaches lies in the use of fracture toughness data measured from deeply cracked specimens tested under bend loading to guarantee high levels of stress triaxiality which drive the fracture process. Under such conditions, a single geometry-independent failure locus then suffices to provide highly effective, albeit conservative, acceptance criteria for cracked structural components. Several flaw assessment methodologies based upon the FAD concept, such as the R6 procedure [4], BS7910 [5], API 579 [6] and SINTAP [7], among others, are now well established and widely employed to analyze the significance of defects in terms of assessment of structural integrity.

Most structural defects are very often part-through surface cracks that form during fabrication or during in-service operation (*e.g.*, blunt corrosion, slag and nonmetallic inclusions, weld cracks, dents at weld seams, etc.) [8]. These crack configurations develop low levels of crack-tip stress triaxiality which contrast sharply to

* Corresponding author.
E-mail addresses: claudio.ruggieri@usp.br, claudio.ruggieri@gmail.com (C. Ruggieri).

http://dx.doi.org/10.1016/j.ijpvp.2014.03.005
0308-0161/

conditions present in deeply cracked specimens. Structural components falling into this category include girth welds made in field conditions for high pressure piping systems and steel catenary risers (SCRs). In particular, as the offshore infrastructure moves into deeper waters, SCRs become more attractive due to their relative low cost, larger diameter and much larger structural capacity when compared to flexible risers. More efficient and faster installation methods are now available which employ the pipe reeling process and allow welding and inspection to be conducted at onshore fabrication facilities (see, *e.g.*, [9,10]). The welded pipe is coiled around a large diameter reel on a vessel and then unreeled, straightened and finally deployed to the sea floor. Undetected crack-like defects in girth welds for these structures are therefore subjected to strong tensile fields associated with large plastic strains which often lead to significant ductile crack extension of a subcritical flaw thereby increasing its size. ECA procedures applicable to reeled pipes [11] rely on the direct application of crack growth resistance ($J-\Delta a$) curves (also often termed R-curves) measured using small, laboratory specimens to specify acceptable flaw sizes. Consequently, the transferability of experimentally measured fracture resistance data to these structural piping components, including pipe girth welds, remains essential in accurate predictions of the in-service residual strength and remaining life.

However, experimental testing of fracture specimens to measure resistance curves consistently reveals a significant effect of specimen geometry, crack size (as characterized by the a/W-ratio) and loading mode (tension *vs.* bending, on R-curves (see Refs. [12–14] for illustrative toughness data)). For the same material, high constraint configurations, such as deeply cracked bend SE(B) and compact tension C(T) specimens, yield low R-curves while shallow-notch bend and predominantly tension loaded configurations develop higher resistance to ductile tearing and larger toughness values at similar amounts of crack growth. This diverse range of ductile fracture behavior under varying constraint conditions has prompted research efforts to incorporate the observed increase in toughness during ductile crack growth in defect assessment procedures of low constraint structures, including circumferentially cracked pipes and cylinders. These approaches rely on the use of single edge notch tension SE(T) specimens under clamp conditions to measure experimental R-curves more applicable to high pressure piping systems, including girth welds of marine steel risers. The primary motivation to use clamped SE(T) fracture specimens in defect assessment procedures for this category of structural components is the similarity in crack-tip stress and strain fields driving the fracture process for both crack configurations as reported in previous studies by Nyhus and co-workers [15–17]. Later, Xu et al. [18,19] examined effects of constraint on ductile crack growth resistance for clamped SE(T) and standard, deeply cracked SE(B) fracture specimens to correlate their fracture response with ductile fracture behavior in circumferentially cracked pipes.

These previous research efforts represent a significant advance in engineering applications of constraint-designed SE(T) fracture specimens directly connected to structural integrity assessments of girth welds in reeled SCRs. Most of these results are derived from comparing SE(T) configurations having varying crack sizes with a standard, deeply-cracked SE(B) specimen with $a/W = 0.5$. Here, the evolving levels of crack-tip constraint with increased remote loading in the SE(T) specimens follow closely the corresponding levels of stress triaxiality for a surface cracked pipe under predominantly tensile loading. It remained apparent, however, that a more systematic investigation on the measuring toughness capacity of these specimens beyond the onset of constraint loss is needed to assess the degree of similarity between SE(T) configurations and circumferentially surface cracked pipes. Nevertheless, recent applications of clamped SE(T) fracture specimens to characterize crack growth resistance properties in pipeline steels [20] have been effective in providing larger flaw tolerances and, at the same time, reducing the otherwise excessive conservatism which arises when measuring the material's tearing resistance based on high constraint specimens.

While now utilized effectively in fracture testing of pipeline girth welds, some difficulties associated with SE(T) testing procedures, including fixture and gripping conditions, may raise concerns about the significance and qualification of measured crack growth resistance curves. Such uncertainties in measured fracture toughness may potentially affect tolerable defect sizes obtained from ECA procedures. While slightly more conservative, testing of shallow-crack bend specimens (which is often viewed as a nonconventional SE(B) configuration) may become more attractive due to its simpler testing protocol, laboratory procedures and much smaller loads required to propagate the crack. Consequently, use of smaller specimens which yet guarantee adequate levels of crack-tip constraint to measure the material's fracture toughness emerges as a highly effective alternative.

Motivated by these observations, this article addresses a two-parameter description of crack-tip fields in bend and tensile fracture specimens incorporating the evolution of near-tip stresses following stable crack growth with increased values of the crack driving force as characterized by the J-integral. The primary objective of this study is twofold. First, the present investigation broadens current understanding on the role of constraint and test conditions in defect assessment procedures for pipeline girth welds using SE(T) and SE(B) specimens. Second, the work addresses the potential coupled effects of geometry and ductile tearing on crack-tip constraint as characterized by the $J-Q$ theory which enables more accurate correlations of crack growth resistance behavior in conventional fracture specimens. Plane-strain and 3-D finite element computations including stationary and growth analyses are conducted for 3P SE(B) and clamped SE(T) specimens having different notch depth (a) to specimen width (W) ratio in the range $0.1 \leq a/W \leq 0.5$. Additional 3-D finite element analyses are also performed for circumferentially cracked pipes with a surface flaw having different crack depth (a) over pipe wall thickness (t) ratios and fixed crack length. For the growth analyses, the models are loaded to levels of J consistent with a crack growth resistance curve, $J-\Delta a$, representative of a typical pipeline steel. A computational cell methodology to model Mode I crack extension in ductile materials is utilized to describe the evolution of J with the accompanying evolving near-tip opening stresses. Laboratory testing of an API 5L X70 steel at room temperature using standard, deeply cracked C(T) specimens is then used to measure the crack growth resistance curve for the material and to calibrate the key cell parameter defined by the initial void fraction, f_0.

2. Overview of the computational cell model for ductile tearing

This section presents a summary of the cell-based framework to model stable crack growth in ductile materials. Further details of the cell model are found in Refs. [21–23]. Ductile fracture in metals is a process of material failure which incorporates various and simultaneous mechanisms at the microscale level [24]. The commonly observed stages of this process are: a) formation of a free surface at an inclusion or second phase particle by either decohesion or particle cracking; b) growth of a void around the particle by means of increased plastic strains and hydrostatic stresses; and c) coalescence of the growing void with adjacent voids. Experimental observations and computational studies show that the plastic strains for nucleation are small thereby causing only little damage in the material ahead of the crack tip. This feature

enables simplification of the ductile failure process by assuming the growth of microvoids as the critical event controlling ductile extension. Fig. 1(a) pictures the schematic path of a growing crack in a ductile material. The material layer enveloping the growing crack, which must be thick enough to include at least a void or microcrack nuclei, identifies a process zone for the ductile fracture which conveniently gives the necessary length dimension for the model. Void growth and coalescence in the layer will cause the surface tractions that the process zone exerts on its surrounding drop to zero (this implicitly defines a traction-separation law for the process zone layer).

Motivated by the above observations, Xia and Shih [21] proposed a model using computational cells to include a realistic void growth mechanism and a microstructural length-scale physically coupled to the size of the fracture process zone. Void growth remains confined to a layer of material symmetrically located about the crack plane, as illustrated in Fig. 1(b), and having thickness D, which is associated with the mean spacing of the larger, void initiating inclusions. This layer consists of cubical cell elements with dimension $D/2$ on each side; each cell contains a cavity of initial volume fraction f_0 (the initial void volume divided by cell volume). As a further simplification, the void nucleates from an inclusion of relative size f_0 immediately upon loading. Progressive void growth and subsequent macroscopic material softening in each cell are described with the Gurson-Tvergaard (GT) constitutive model for dilatant plasticity [25,26] given by

$$\left(\frac{\sigma_e}{\overline{\sigma}}\right)^2 + 2q_1 f \cosh\left(\frac{3q_2\sigma_m}{2\overline{\sigma}}\right) - \left(1 - q_3 f^2\right) = 0 \qquad (1)$$

where σ_e denotes the effective Mises (macroscopic) stress, σ_m is the mean (macroscopic) stress, $\overline{\sigma}$ is the current flow stress of the cell matrix material and f defines the current void fraction. Factors q_1, q_2 and $q_3 = q_1^2$ introduced by Tvergaard [26] improve the model predictions for periodic arrays of cylindrical and spherical voids. In the analyses addressed later for an API 5L X70 grade pipeline steel, improved q-values derived from the work of Faleskog and Shih [27] are used; these q-values are applicable to a wide range of material flow properties (strain hardening properties and yield stress) for common pressure vessel and structural steels. Using an experimental $J-\Delta a$ curve obtained from a conventional, deeply cracked SE(B) or C(T) specimen, a series of finite element analyses of the specimen are conducted to calibrate values for the cell parameters D and f_0 which bring the predicted $J-\Delta a$ curve into agreement with experiments as described later in the article.

Further improvement in the cell methodology introduced by Ruggieri and Dodds (R&D) [22] and Gullerud et al. [23] enables the model to create new traction free surfaces to represent physical crack extension. When f in the cell incident on the current crack tip reaches a critical value, f_E, the computational procedures remove the cell thereby advancing the crack tip in discrete increments of the cell size (Tvergaard [26] refers to this process as the element extinction or vanish technique). R&D [22] and Gullerud et al. [23] implements a cell extinction process using a linear-traction separation model with the critical porosity typically assigned a value of $f_E = 0.15 \sim 0.20$. The final stage of void linkup with the macroscopic crack front then occurs by reducing the remaining stresses to zero in a prescribed linear manner.

3. Description of constraint variation in fracture

Much research in the last years has convincingly demonstrated the strong effects of specimen geometry and loading mode (bending *vs.* tension) on fracture behavior for ferritic structural steels in the ductile-to-brittle (DBT) transition region as well as in the upper shelf region. At increased loads in a finite body, such as a cracked specimen or structure, the initially strong small scale yielding (SSY) fields gradually change to fields under large scale yielding (LSY) as crack-tip plastic zones increasingly merge with the

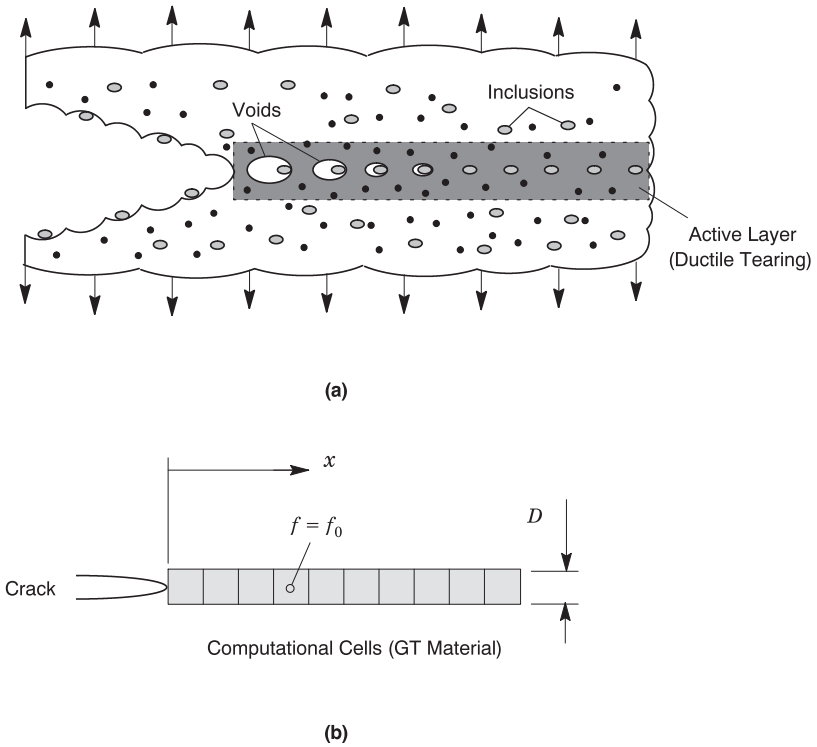

Fig. 1. Modeling of ductile tearing using computational cells.

global bending plasticity on the nearby traction free boundaries. This phenomenon, often termed loss of constraint, contributes to the apparent increased toughness of shallow cracked and tension loaded geometries observed in fracture testing [28,29].

While a number of approaches have been proposed to describe effects of constraint changes on fracture behavior, the present work focuses on a widely adopted methodology to quantify the evolving level of stress triaxiality ahead of the crack front under increased remote loading based upon the J–Q framework. This section introduces the essential features of the methodology needed to correlate fracture behavior in circumferentially cracked pipes and cylinders and common fracture specimens, including the SE(B) and SE(T) configurations with varying crack sizes. Attention is directed first to conditions pertaining to stationary cracks subjected to monotonically increasing loading (deformation). Subsequent development focuses on a simpler extension of the J–Q approach to steady-state growing cracks.

3.1. Constraint measures in stationary cracks: the J–Q approach

Development of a two-parameter characterization of the elastic–plastic crack-tip fields begins by considering a cracked body subjected to a remote stress in which crack-tip deformation scales with J/σ_0 where J denotes Rice's J-integral [30] and σ_0 is a reference (yield) stress. At load levels sufficiently small so that crack-tip plasticity is limited, it can be shown that the mode I plane-strain elastic–plastic near-tip fields can be described by a single family of crack-tip fields with varying stress triaxiality. These arguments motivated O'Dowd and Shih (OS) [31,32] to propose an approximate two-parameter description for the elastic–plastic crack tip fields based upon a triaxiality parameter more applicable under large scale yielding (LSY) conditions for materials with elastic–plastic response described by a power hardening law given by $\varepsilon/\varepsilon_0 \propto (\sigma/\sigma_0)^n$. Here, n denotes the strain hardening exponent, σ_0 and ε_0 are the reference (yield) stress and strain, respectively. Guided by detailed numerical analyses employing a modified boundary layer (MBL) model, originally proposed by Rice [33], OS [31,32] identified a family of self-similar fields in the form

$$\sigma_{ij} = \sigma_0 f_{ij}\left(\frac{r}{J/\sigma_0},\ \theta,\ Q\right) \tag{2}$$

where the dimensionless second parameter Q defines the amount by which σ_{ij} in fracture specimens differ from the adopted reference SSY solution with the T-stress term [34–37] set to zero. In the above Eq. (2), r and θ are polar coordinates centered at the crack tip with $\theta = 0$ corresponding to a line ahead of the crack.

Limiting attention to the forward sector ahead of the crack tip between the SSY and the fracture specimen fields, OS showed that $Q\sigma_0$ corresponds effectively to a spatially uniform hydrostatic stress, i.e., the difference field relative to a high triaxiality reference stress state

$$(\sigma_{ij})_{\mathrm{FB}} = (\sigma_{ij})_{\mathrm{SSY}} + Q\sigma_0\delta_{ij} \tag{3}$$

where the dimensionless second parameter Q defines the amount by which σ_{ij} in fracture specimens, $(\sigma_{ij})_{\mathrm{FB}}$, differ from the adopted high triaxiality reference SSY solution, $(\sigma_{ij})_{\mathrm{SSY}}$. Consequently, Q is often defined as

$$Q \equiv \frac{(\sigma_{yy})_{\mathrm{FB}} - (\sigma_{yy})_{\mathrm{SSY}}}{\sigma_0} \tag{4}$$

where the difference field described in terms of the opening (Mode I) stresses, σ_{yy}, is conventionally evaluated at the normalized crack-tip distance $\bar{r} = r/(J/\sigma_0) = 2$, which represents a microstructurally significant distance ahead of crack tip related to the operative fracture mechanism. OS [31,32] and Cravero and Ruggieri [38] have also shown that Q is relatively independent of r in the range $1 \le \bar{r} \le 5$. Construction of J–Q trajectories for structural components and fracture specimens then follows by evaluation of Eq. (4) at each stage of loading in the finite body. Fig. 2(a) depicts the procedure to determine parameter Q for a moderate hardening material simply as the difference field at a given near-tip location; here, the computed difference between the SSY reference field and the near-tip (opening) stress for the finite body gradually increases with increasing remote loading as characterized by J. At similar values of the continuum, scalar parameters (J, Q), the crack-tip strain-stress fields which drive the local process have similar values as well.

3.2. Extension of the J–Q approach for growing cracks

While the above framework was essentially developed for stationary cracks, the two-parameter description of near-tip stress states based on the constraint parameter, Q, can be extended to a steadily growing crack in a straightforward manner. Based upon the interpretation of Q as a measure of the level of stress triaxiality that quantifies the difference field relative to a high triaxility reference stress state for a stationary crack ($\Delta a = 0$), an alternative form applicable to growing cracks, denoted as $\widehat{Q}$ in the present work, can be defined as

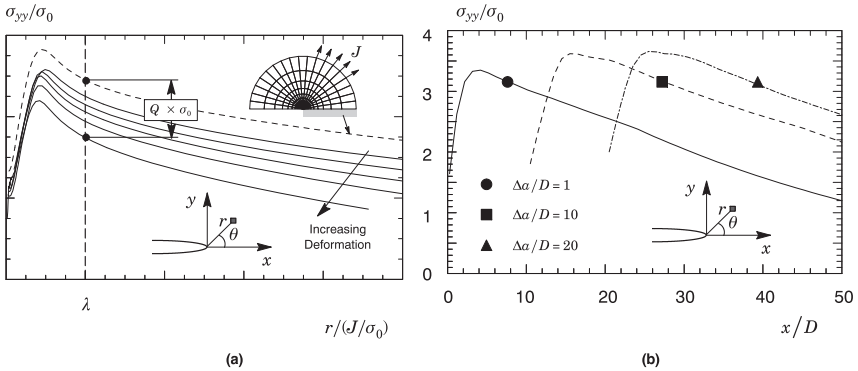

Fig. 2. (a) Procedure to determine parameter Q based on the difference field at a given near-tip location; (b) Schematic representation of the evolving near-tip (opening) stresses with increased amounts of ductile tearing.

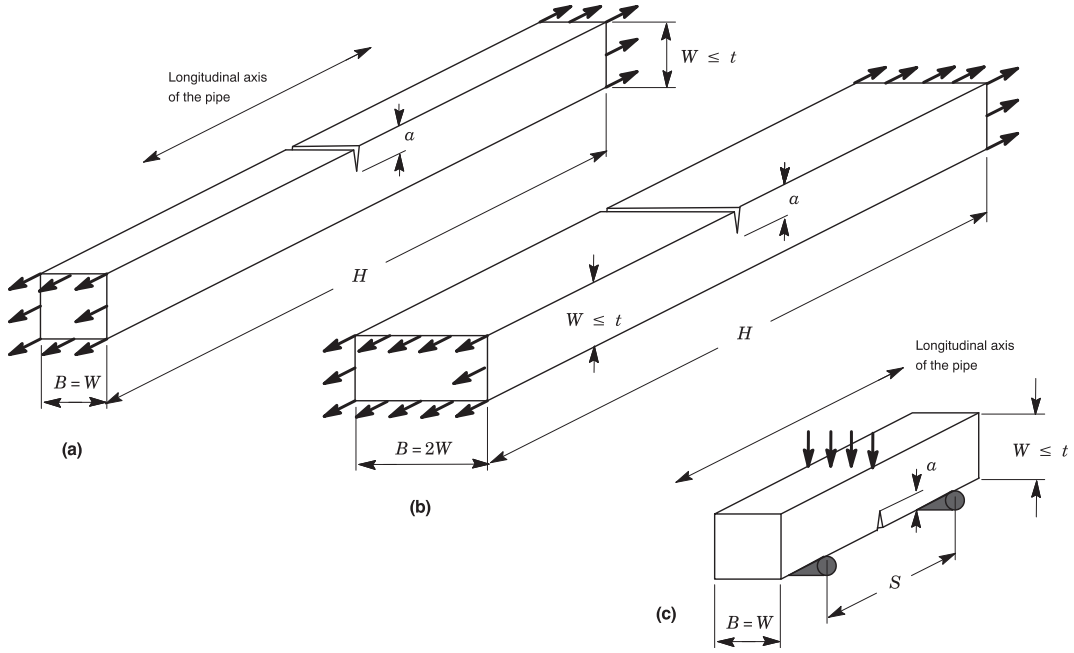

Fig. 3. Geometry and specimen dimensions for the analyzed crack configurations.

$$\widehat{Q} \equiv \frac{(\sigma_{yy})^{\Delta a}_{\mathrm{FB}} - (\sigma_{yy})^{\Delta a=0}_{\mathrm{SSY}}}{\sigma_0} \tag{5}$$

where the difference field described is now evaluated at the *current* normalized crack-tip distance, $\widehat{r} = 2J/\sigma_0$, which represents the location of a material point ahead of the advancing crack tip.

Fig. 2(b) shows the evolving near-tip (opening) stresses with increased amounts of ductile tearing, Δa, represented as a multiple of the cell size, D, for a moderate hardening material. Clearly, the tensile stress ahead of crack tip changes steadily with crack growth (compare the stress distributions for $\Delta a/D = 1$ and $\Delta a/D = 10$) thereby altering the corresponding levels of constraint (as measured by $\widehat{Q}$) with increased crack extension. These observations are entirely consistent with the previous investigation of Varias and Shih [39] and Dodds et al. [40] in which crack growth under well-contained yielding changes near-tip constraint. This issue is addressed in more details later in the article.

4. Numerical procedures and material models

4.1. Finite element models of fracture specimens for stationary crack analyses

Nonlinear finite element analyses are described for plane-strain models of bend and tension loaded crack configurations covering plane-sided SE(B) and SE(T) fracture specimens with fixed geometry having thickness $B = 20.6$ mm and varying crack sizes. The

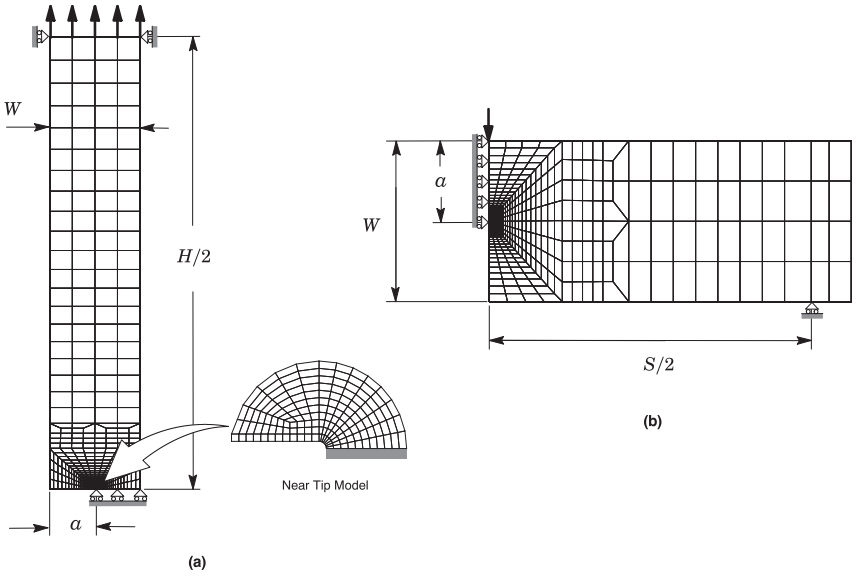

Fig. 4. Finite element models used in plane-strain analyses of fracture specimens; (a) 3P SE(B) specimen with $a/W = 0.5$; (b) Clamped SE(T) specimen with $a/W = 0.5$ and $H/W = 10$.

analysis matrix includes SE(B) specimens ($S/W = 4$) and clamped SE(T) specimens ($H/W = 10$) with $W/B = 1$ (often referred to as $B \times B$ configuration) having $a/W = 0.1$ to 0.5 with increments of 0.1. Here, a is the crack size, W is the specimen width, S defines the specimen span for the bend configuration and H represents the distance between clamps for the tension specimen. These crack configurations are extracted from the longitudinal direction of pipes having wall thickness, t, and often utilized to measure fracture toughness properties in pipeline girth welds subjected to reeling. Fig. 3 shows the geometry and specimen dimensions for the analyzed crack configurations which also includes a clamped SE(T) configuration with $W/B = 0.5$ utilized in the 3-D analyses described later.

Fig. 4(a–b) shows the finite element models constructed for the plane-strain analyses of the SE(B) and clamped SE(T) specimen having $a/W = 0.5$. All other crack models have very similar features. A conventional mesh configuration having a focused ring of elements surrounding the crack front is used with a small key-hole at the crack tip; the radius of the key-hole, ρ_0, is 2.5 μm (0.0025 mm) to enhance computation of J-values at low deformation levels. Previous numerical analyses [38] reveal that such mesh design provides detailed resolution of the near-tip stress-strain fields which is needed for accurate numerical evaluation of J-values. Symmetry conditions permit modeling of only one-half of the specimen with appropriate constraints imposed on the remaining ligament. A typical half-symmetric model has one thickness layer of 1300 8-node, 3D elements (~2800 nodes) with plane-strain constraints ($w = 0$) imposed on each node. These finite element models are loaded by displacement increments imposed on the loading points to enhance numerical convergence.

Finite element analyses are also conducted on numerical models in full 3-D setting for the clamped SE(T) and SE(B) fracture specimens with $W/B = 1$ described previously. The analysis matrix includes the same crack configurations as defined before covering $a/W = 0.1$ to 0.5 with increments of 0.1. To assess the effects of thickness on fracture behavior, the 3-D numerical computations are also performed on finite element models for the clamped SE(T) specimen with $W/B = 0.5$; this crack configuration is recommended by DNV F-108 procedure [41] for experimental measurements of crack growth resistance curves in pipeline steels and their weldments using fracture specimens extracted from the longitudinal direction of the pipe. Fig. 5(a–b) shows the finite element models constructed for the 3-D analyses of the clamped SE(T) and SE(B) specimens with $W/B = 1$ and $a/W = 0.5$. Again, a conventional mesh configuration having a focused ring of elements surrounding the crack front is used with a small key-hole at the crack tip where the radius of the key-hole, ρ_0, is also 2.5 μm (0.0025 mm). Symmetry conditions permit modeling of only one-quarter of the specimen with appropriate constraints imposed on the remaining ligament. A typical quarter-symmetric, 3-D model has 20 variable thickness layers with ~25,000 8-node, 3D elements (~30,000 nodes) defined over the half-thickness ($B/2$); the thickest layer is defined at $Z = 0$ with thinner layers defined near the free surface ($Z = B/2$) to accommodate the strong Z variations in the stress distribution. These numerical models are loaded by displacement increments imposed on the loading points to enhance numerical convergence with increased levels of deformation. The 3-D finite element models for the SE(T) specimens with $W/B = 0.5$ have also similar features as the 3-D crack models for the clamped SE(T) and SE(B) fracture specimens with $W/B = 1$.

4.2. Numerical models of circumferentially cracked pipes

Nonlinear 3-D finite element analyses are performed on circumferentially cracked pipes with external surface flaws subjected to reeling. The analyzed pipe models have wall thickness $t = 20.6$ mm with outside diameters $D_e = 309$ mm ($D_e/t = 15$). This geometry typifies current trends in deep water submarine pipelines and risers made of high grade pipeline steels. The analysis matrix considers surface, semi-elliptical flaws with varying crack depth (a) and crack length ($2c$) as defined by $a/t = 0.1$ to 0.4 with increments of 0.1, and $2c = 196$ mm ($11.9 \leq c/a \leq 47.6$), which corresponds to $\theta/\pi = c/(2D_e) = 0.16$ according to API 579 [6]. Fig. 6(a) illustrates the adopted scheme for the numerical simulation of reeling with the reel drum being modeled by a rigid surface with diameter $D_r = 15{,}000$ mm; in the figure, the vertical displacement, V, represents the load line displacement (LLD). Fig. 6(b) shows the pipe configuration and defect geometry adopted in the numerical analyses; here, we note that the semi-elliptical flaw geometry is slightly degenerated to accommodate the pipe curvature as shown in Fig. 6(c). The adopted pipe geometry and reel drum diameter produce plastic strain levels of ~2 % in the outermost radius during

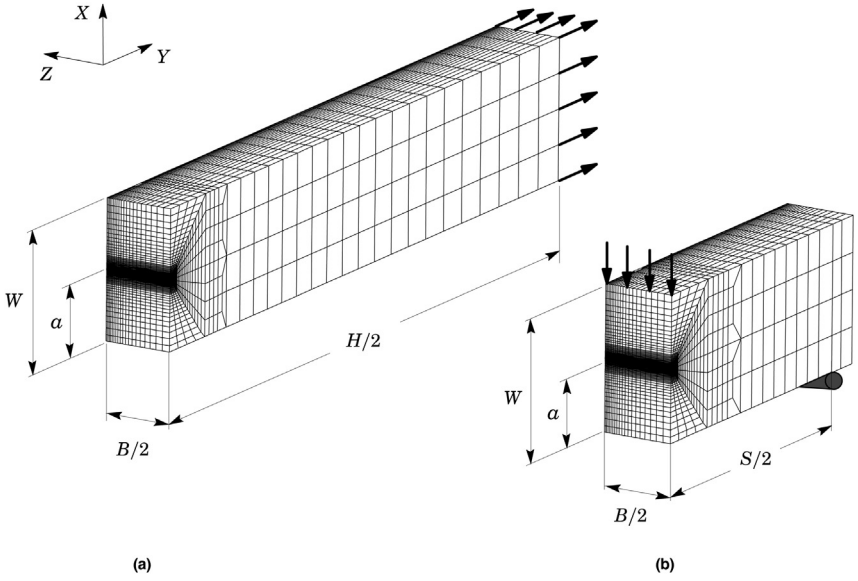

Fig. 5. 3-D Finite element models of fracture specimens; (a) 3P SE(B) specimen with $a/W = 0.5$; (b) Clamped SE(T) specimen with $a/W = 0.5$ and $H/W = 10$.

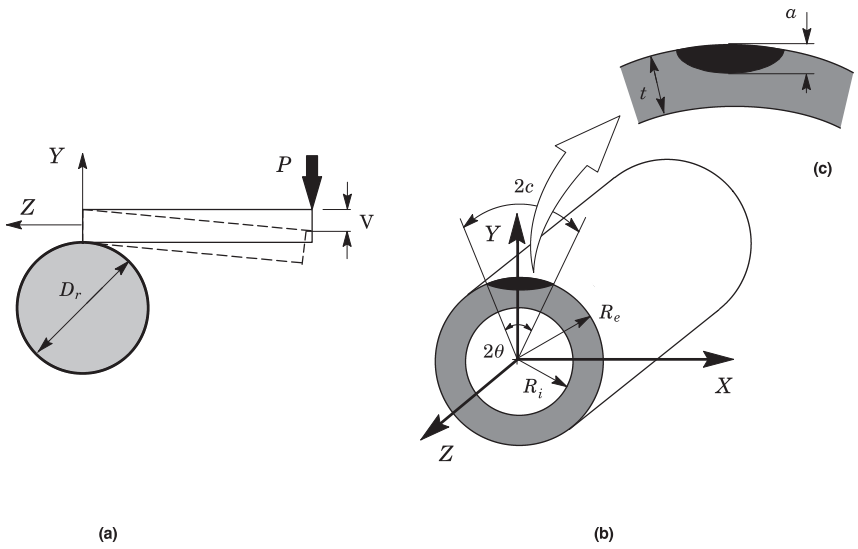

Fig. 6. (a) Adopted scheme for the numerical simulation of pipe reeling; (b) Pipe configuration and defect geometry adopted in the numerical analyses; (c) Illustration of the semi-elliptical geometry representing the circumferential surface flaw of the pipe.

the reeling process which is in accord with current guidelines for submarine pipeline installation [11]. Additional analyses for circumferentially cracked pipes with $2c = 98$ mm ($5.9 \leq c/a \leq 23.8$) were also conducted; however, since their fracture response in terms of J–Q trajectories is essentially similar to the numerical models with $2c = 196$ mm, the results for the shorter flaw are omitted to conserve space in the present work.

Fig. 7 shows the finite element model constructed for the pipe with $a/t = 0.4$ and $2c = 196$ mm ($c/a = 11.9$). The numerical models for the circumferentially cracked pipes also employ a conventional mesh configuration having a focused ring of elements surrounding the crack front with a small key-hole geometry (blunt tip) at the crack tip ($\rho_0 = 0.0025$ mm). The half-symmetric models for these analyses have ~67,000 8-node, 3-D elements (~78,000 nodes) with appropriate constraints imposed on nodes defining the longitudinal symmetry plane. The crack front is described by 30 (circumferential) layers defined over the crack half-length (c); the thickest layer is defined at the deepest point of the crack with thinner layers defined near the free surface to accommodate the strong gradient in the stress distribution along the crack front.

4.3. Finite element models of the fracture specimens and circumferentially cracked pipes including ductile tearing

The extensive set of crack growth analyses described in the present study explores the effects of ductile tearing on constraint variations for the circumferentially cracked pipes and fracture specimens previously described. For these analyses, a mesh with computational cells ahead of crack front (see Section 2) is used in 3-D settings consistent with the previous numerical models for stationary crack solutions. Moreover, the arrangement of cell elements ahead of the Mode I growing crack follows closely the scheme depicted in Fig. 1(b). Experience with past finite element analyses of fracture specimens to estimate the cell size for common structural

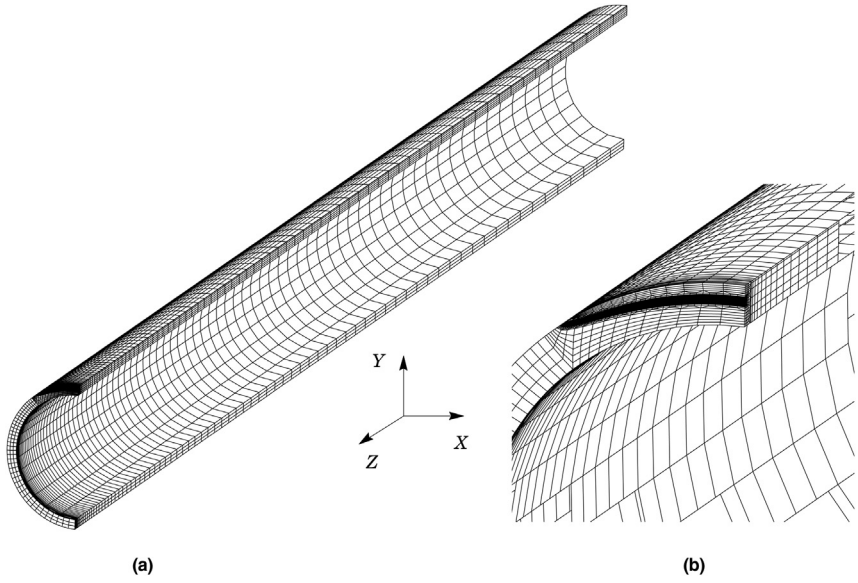

Fig. 7. (a) 3-D finite element model employed for the pipe configuration with $D_e/t = 15$, $a/t = 0.4$ and $c/a = 11.9$; (b) Near-tip model and meshing details.

and pressure vessel steels suggests values of 50∼200 μm for D [22,23,42]. Here, the cell size is adopted as $D/2 = 100$ μm. This size provides an approximate correlation of spacing between the large inclusions and the crack tip opening displacement (CTOD) at the onset of macroscopic crack growth in conventional fracture specimens for common pressure vessel steels while, at the same time, providing adequate resolution of the stress-strain fields in the active layer and in the adjacent background material.

To simulate ductile crack extension using the GT model, the planar meshes (2-D) for the SE(T) and SE(B) fracture specimens contains a row of 60 computational cells along the remaining crack ligament ($W-a$). The 3-D numerical models for these crack configurations are obtained by simply extruding the 2-D mesh along the Z-axis. Symmetry conditions enable analyses using one-quarter of the specimen with appropriate constraints imposed on the symmetry planes. These numerical models have 14 variable thickness layers defined over the half-thickness ($B/2$) with the thickest layer defined at $Z = 0$. The quarter-symmetric, 3-D models for these specimens have ∼38,000 nodes and ∼38,000 elements with $60 \times 14 = 840$ computational cells ahead of crack front.

Nonlinear 3-D finite element analyses including ductile tearing are also performed on circumferentially cracked pipes with $D_e = 309$ mm and $t = 20.6$ mm (D_e/t=15) having an external surface flaw with $2c = 196$ mm and $a/t = 0.2$, 0.3 and 0.4 (see Fig. 6). The crack front is described by 30 (circumferential) layers defined over the crack half-length (c); for each crack front layer, a row of 60 computational cells is arranged over the remaining crack ligament ($t-a$) thereby enabling description of ductile crack extension along the crack front. The half-symmetric models for these analyses have ∼60,000 8-node, 3-D elements (∼68,000 nodes) with appropriate constraints imposed on nodes defining the longitudinal symmetry plane.

Calibration of the initial material porosity (void fraction), f_0, for the GT material requires a crack growth analysis to match R-curves obtained from testing of high constraint, deeply cracked specimens. Hippert [43] tested 1-T compact tension C(T) specimens ($B = 25.4$ mm) with $a/W = 0.65$ and 20% side-grooves (10% each side) to measure ductile tearing properties for the API X70 pipeline steel described next. Ideally, the growth analysis for this specimen should employ full 3-D numerical finite element models incorporating an arrangement of cell elements ahead of the 3-D crack front. However, previous studies of Ruggieri and Doods [22] revealed that analyses of ductile crack extension using 3-D computational cells exhibit significant problems related to meshing and physical growth by cell extinction along the crack plane. In particular, the side-groove region in the numerical model suppresses crack growth thereby making it difficult to define a meaningful computed resistance curve against which the experimentally measured R-curve is compared to determine the key parameter, f_0. Since our primary interest lies in the assessment of constraint effects in cracked pipes and fracture specimens including ductile tearing, the characterization of crack growth response evaluated at the centerplane of the crack configuration (Z=0) proves adequately effective. Moreover, a number of previous works, including the numerical investigation of Nevalainen and Dodds [29], demonstrated the relatively small effects of side grooves on midplane constraint for common specimen geometries. Hence, in this case it suffices to consider a plane-strain model to simulate ductile crack extension for the tested C(T) specimen such that the computed R-curve describes well the experimentally measured crack growth response. The finite element mesh for the growth analysis of the deeply-cracked C(T) specimen contains a row of 120 computational cells along the remaining crack ligament ($W-a$) with fixed size of $D/2 \times D/2$ (see Fig. 1(b)). The initially blunted crack tip accommodates the intense plastic deformation and initiation of stable crack growth in the early part of ductile tearing. Symmetry conditions permit modeling of only one-half of the specimen with appropriate constraints imposed on the remaining ligament. This half-symmetric, plane-strain model has one thickness layer of 1611 8-node, 3D elements (3522 nodes) with plane-strain constraints (w=0) imposed on each node and displacement increments imposed on the loading point which permits continuation of the analyses once the load decreases during crack growth.

4.4. Material models and finite element procedures

The elastic–plastic constitutive model employed in all stationary crack analyses reported here follows a flow theory with conventional Mises plasticity in small geometry change (SGC) setting. The numerical solutions for fracture specimens and cracked pipes utilize a simple power-hardening model to characterize the uniaxial true stress ($\overline{\sigma}$) *vs.* logarithmic strain ($\overline{\varepsilon}$) in the form

$$\frac{\overline{\varepsilon}}{\varepsilon_0} = \frac{\overline{\sigma}}{\sigma_0}, \varepsilon \le \varepsilon_0; \frac{\overline{\varepsilon}}{\varepsilon_0} = \left(\frac{\overline{\sigma}}{\sigma_0}\right)^n, \varepsilon > \varepsilon_0 \tag{6}$$

where σ_0 and ε_0 are the reference (yield) stress and strain, and n is the strain hardening exponent. The finite element analyses consider material flow properties covering typical structural, pressure vessel and pipeline grade steels with $E = 206$ GPa and $\nu = 0.3$: $n = 5$ and $E/\sigma_0 = 800$ (high hardening material), $n = 10$ and $E/\sigma_0 = 500$ (moderate hardening material), $n = 20$ and $E/\sigma_0 = 300$ (low hardening material). These ranges of properties also reflect the upward trend in yield stress with the increase in strain hardening exponent, n, characteristic of ferritic structural steels, including pipeline steels.

For the crack growth analyses, the mechanical and flow properties for an API 5L X70 pipeline grade steel described next are employed to generate the required numerical solutions in large geometry change (LGC) setting. The material has 484 MPa yield stress (σ_{ys}) and 590 MPa tensile strength (σ_{uts}) at room temperature (20 °C) with relatively moderate-to-low hardening properties ($\sigma_{uts}/\sigma_{ys} \approx 1.22$), Young's modulus $E = 205$ GPa and Poisson's ratio $\nu = 0.3$. Fig. 8 shows the engineering stress-strain curve for the tested steel (average of two tests) obtained from mechanical tensile tests conducted on longitudinal tensile specimens (ASTM E8 [44]) at room temperature (20 °C). Using these tensile properties and an improved estimate for the hardening exponent given by Annex F of

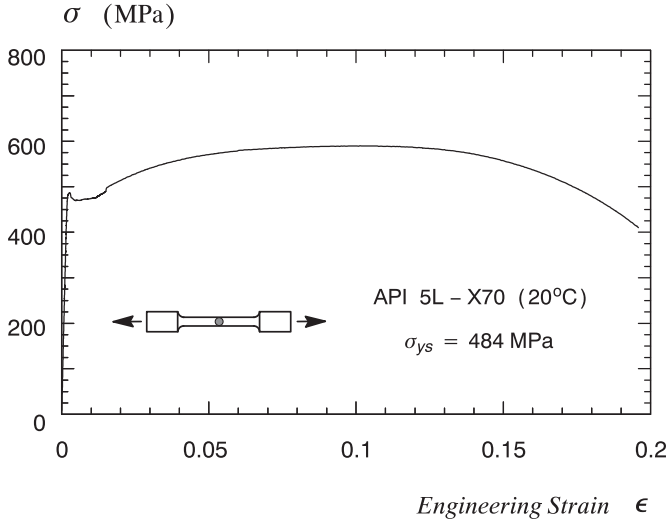

Fig. 8. Engineering stress-strain curve for the tested API 5L X70 pipeline steel [43,49].

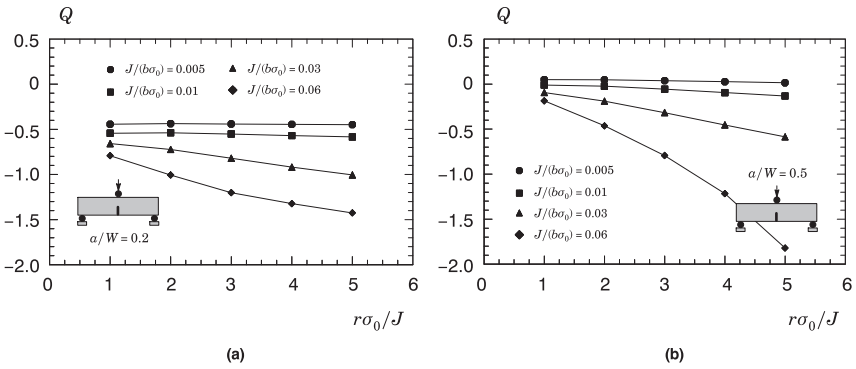

Fig. 9. Variation of parameter Q with normalized crack-tip distance for the SE(B) specimen with $n = 10$ ($E/\sigma_0 = 500$) material: (a) $a/W = 0.2$; (b) $a/W = 0.5$.

API 579 [6], the strain hardening exponent for the adopted API 5L X70 pipeline grade steel yields $n = 13.3$ thereby closely characterizing a moderate hardening behavior material.

To describe the evolution of void growth and associated macroscopic material softening in the computational cells, the GT constitutive model given by Eq. (1) is adopted. The background material outside of the computational cells follows a flow theory with the Mises plastic potential obtained by setting $f \equiv 0$ in Eq. (1). The uniaxial true stress-logarithmic strain response for both the background and cell matrix materials follows a piecewise linear approximation to the measured tensile response for the material at room temperature shown in Fig. 8. The two adjustment factors in the Gurson yield condition given by Eq. (1) are taken as $q_1 = 1.43$ and $q_2 = 0.97$ in the present analyses. These q-values are derived from the work of Faleskog and Shih [27] which provides the adjustment parameters q_1 and q_2 for a wide range of material flow properties (strain hardening properties and yield stress) for common pressure vessel and structural steels.

The finite element code WARP3D [45] provides the numerical solutions for the plane-strain and 3-D simulations reported here including stationary and crack growth analyses implementing the cell model. Evaluation of the J-integral derives from a domain integral procedure which yields J-values in excellent agreement with estimation schemes based upon η-factors for deformation plasticity in the fracture specimens [46] while, at the same time, retaining strong path independence for domains defined outside the highly strained material near the crack. WARP3D analyzes fracture models constructed with three-dimensional, 8-node trilinear hexahedral elements. To achieve plane-strain conditions for the current study, a single thickness layer of the 3-D elements is defined with out-of-plane displacements constrained to vanish. The research code FRACTUS2D [47] is employed to compute J–Q and $J - \widehat{Q}$ curves derived from stationary and growing analyses for the analyzed fracture specimens and circumferentially cracked pipes.

5. Evolution of crack-tip constraint in stationary cracks

Previous studies [28,29,38,48] have characterized crack-front stress fields for common fracture specimens using the J–Q methodology to quantify effects of constraint loss on fracture behavior. Here, we enlarge on these previous developments to examine in more detail the constraint variations in terms of J–Q trajectories derived from the extensive analyses conducted on SE(B) and clamped SE(T) fracture specimens and also on circumferentially cracked pipes with varying crack sizes and hardening behavior. The section begins with descriptions of crack front constraint for SE(B) and clamped SE(T) specimens under plane-strain conditions. These analyses are followed by a 3-D characterization of J–Q trajectories using detailed 3-D models for these crack configurations. The presentation concludes with 3-D results describing the evolution of Q with increased J-values for the circumferentially cracked pipes under reeling.

5.1. Plane-strain results for SE(B) and clamped SE(T) fracture specimens

The J–Q trajectories to be presented next are computed at the particular distance $\bar{r} = r/(J/\sigma_0) = 2$. Since Q is a measure of the deviation in the stress fields for the finite cracked body from the reference SSY fields, we first examine the variation of the constraint parameter, Q, with crack-tip distance. Figs. 9,10 show Q-values computed at varying normalized distances, $r/(J/\sigma_0)$, for the shallow

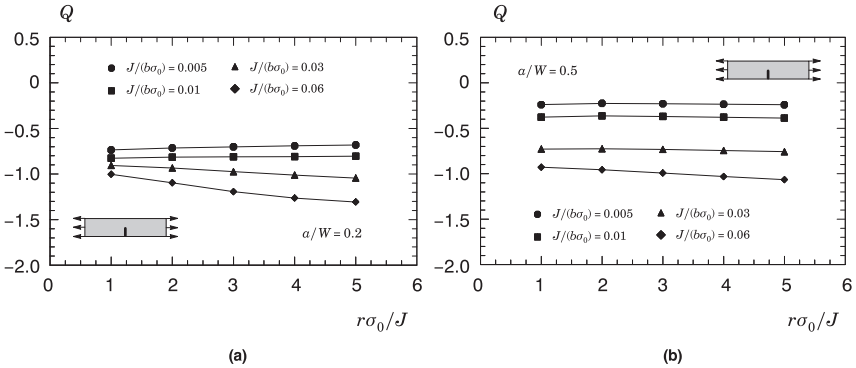

Fig. 10. Variation of parameter Q with normalized crack-tip distance for the clamped SE(T) specimen with $n = 10$ ($E/\sigma_0 = 500$) material: (a) $a/W = 0.2$; (b) $a/W = 0.5$.

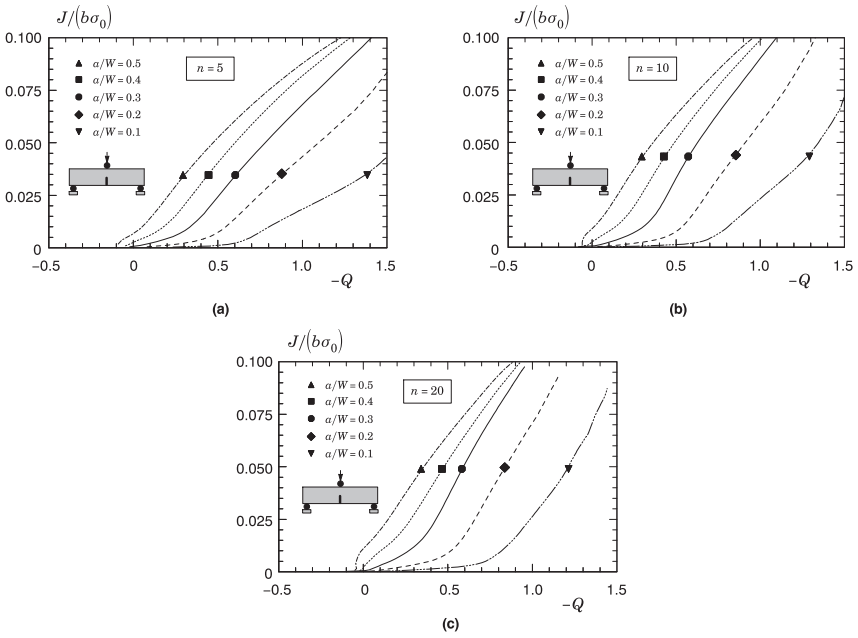

Fig. 11. Plane-strain J–Q trajectories for the SE(B) specimen with different crack sizes and varying material properties: (a) $n = 5$ ($E/\sigma_0 = 800$); (b) $n = 10$ ($E/\sigma_0 = 500$); (c) n=20 (E/σ_0=300).

and deeply cracked SE(B) and SE(T) fracture specimens with the moderate hardening ($n = 10$) material ($E/\sigma_0 = 500$) at increased deformation. The Q-values for the shallow crack SE(B) and the clamped SE(T) specimens displayed by these plots show a relatively weak radial dependence under increasing loading, particularly for the tension loaded configuration. In contrast, parameter Q for the deeply cracked SE(B) specimen shown in Fig. 9(b) displays consistently increased radial dependence under increasing loading, particularly for large applied J-values. This behavior reflects the interaction of the remote plastic bending field acting on the remaining ligament ($b = W–a$) which impinges strongly upon the crack tip resulting in steeper stress gradients at higher deformation levels. Such trends are consistent with previous analyses of O'Dowd and Shih (OS) [31,32], Nevalainen and Dodds [29] and Cravero and Ruggieri [38]. Similar results hold across all other crack configurations and hardening properties thereby providing reasonable support to the value $\bar{r} = 2$ adopted in the present work; to conserve space, they are not shown here.

Figs. 11, 12 display the general effects of specimen geometry, loading mode and flow properties on the J–Q trajectories for the analyzed crack configurations. In all plots, Q is defined by Eq. (4) at the normalized crack-tip distance given by $\bar{r} = 2$ whereas J is

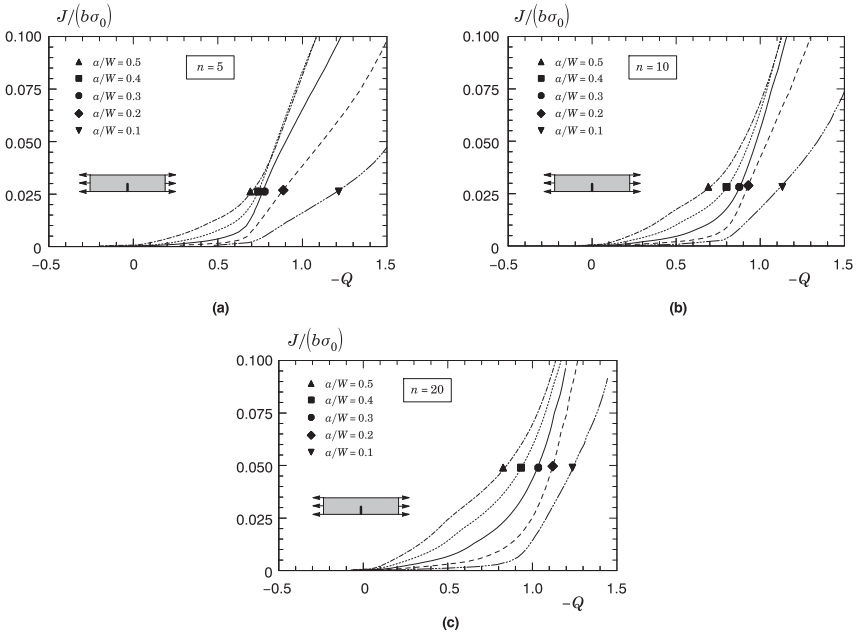

Fig. 12. Plane-strain J–Q trajectories for the clamped SE(T) specimen with different crack sizes and varying material properties: (a) $n = 5$ ($E/\sigma_0 = 800$); (b) $n = 10$ ($E/\sigma_0 = 500$); (c) $n = 20$ ($E/\sigma_0 = 300$).

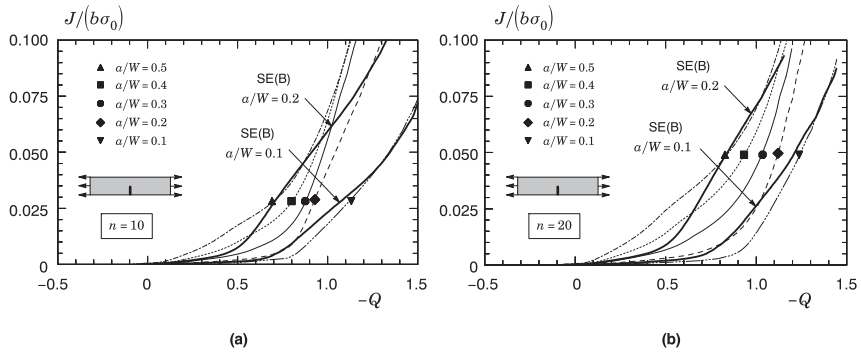

Fig. 13. Comparison of plane-strain $J-Q$ trajectories for the clamped SE(T) crack configuration with varying crack sizes and shallow notch SE(B) specimens: (a) $n = 10$; (b) $n = 20$.

normalized by $b\sigma_0$ with b denoting the remaining crack ligament $W-a$ (notice that we plot $J/b\sigma_0$ vs. $-Q$ to maintain positive scales). For each crack configuration, the evolution of Q depends markedly on crack size, as characterized by the a/W-ratio, particularly for the SE(B) specimen. For this specimen configuration, there is a rather uniform shift of the $J-Q$ trajectories with decreased crack size. In contrast, the evolution of Q with $J/b\sigma_0$ for the clamped SE(T) specimen displays much less sensitivity on crack size in the range $a/W \geq 0.3$, particularly for the high hardening material. These specimens also show large negative Q-values almost immediately upon loading for all strain hardening properties which are associated with substantial reduction in the opening near-tip stresses early in the loading.

An interesting result having a direct bearing on experimental evaluation procedures of crack growth resistance properties in pipelines is the strong correlation between the $J-Q$ trajectories for the shallow crack SE(B) specimen with $a/W = 0.1$ and 0.2, and the clamped SE(T) specimen with varying a/W-ratios. Fig. 13 recasts the previous crack front constraint variations to provide selected $J-Q$ trajectories for the $n = 10$ and $n = 20$ materials. It is clear that both shallow crack SE(B) specimens and clamped SE(T) configurations display similar descriptions of crack front constraint with increased deformation.

5.2. 3-D results for SE(B) and clamped SE(T) fracture specimens

Conventional plane-strain, 2-D analyses provide $J-Q$ trajectories that do not reflect the effects of out-of-plane constraint on the near-tip opening stresses. 3-D analyses describe more adequately the through-thickness variations in crack front stresses with consequent impact on Q-values over the crack front, including the center portion of the specimen thickness. Here, we provide descriptions of crack front constraint corresponding to the midplane location in the SE(B) and SE(T) specimens. Since a primary interest of the present work lies in the fracture correlation between common specimens and a circumferentially cracked pipeline, we can advantageously evaluate the dependence of Q on J at the crack front location defined by $Z/(B/2) = 0$ for subsequent comparisons with the $J-Q$ trajectories evaluated at the deepest point of the circumferential surface crack in the reeled pipe addressed next.

Figs. 14, 15 show the evolution of parameter Q evaluated at the crack-tip distance given by $\bar{r} = 2$ with increased deformation for the SE(B) and SE(T) specimens with $W/B = 1$ and varying crack sizes and hardening behavior. As already mentioned, these $J-Q$ trajectories correspond to the midplane location so that Q derives from Eq. (4) in which the opening stresses, $(\sigma_{yy})_{FB}$, are evaluated at $Z/(B/2) = 0$. The general trends already observed previously for the

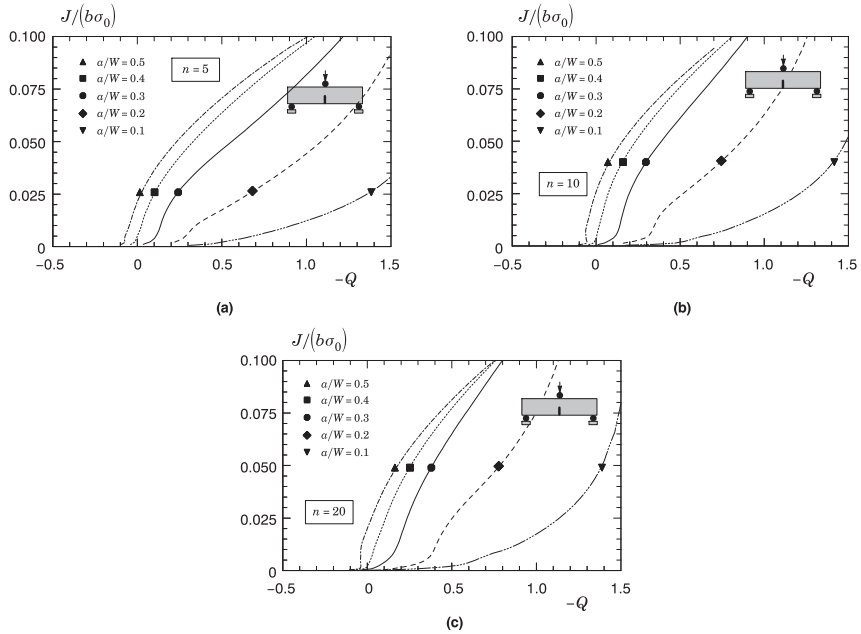

Fig. 14. $J-Q$ trajectories evaluated at midplane specimen for the SE(B) configuration with $W/B = 1$ and different crack sizes and varying material properties: (a) $n = 5$ ($E/\sigma_0 = 800$); (b) $n = 10$ ($E/\sigma_0 = 500$); (c) $n = 20$ ($E/\sigma_0 = 300$).

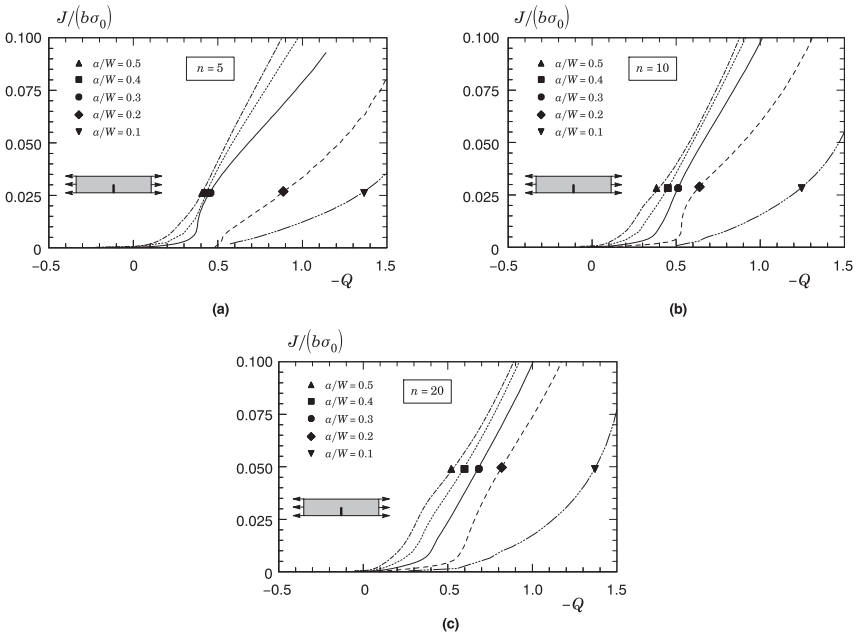

Fig. 15. $J-Q$ trajectories evaluated at midplane specimen for the clamped SE(T) configuration with $W/B = 1$ and different crack sizes and varying material properties: (a) $n = 5$ ($E/\sigma_0 = 800$); (b) $n = 10$ ($E/\sigma_0 = 500$); (c) $n = 20$ ($E/\sigma_0 = 300$).

plane-strain results remain essentially unchanged. Moreover, examination of these plots reveals that the midplane location of the 3-D model maintains higher levels of constraint with increased deformation for both configurations in the crack size range $a/W \geq 0.3$ for the SE(B) specimen and $a/W \geq 0.2$ for the clamped SE(T) specimen. Observe that the Q-value at a given $J/(b\sigma_0)$ is somewhat higher for these configurations compared to the plane-strain results. Fig. 16 compares selected $J-Q$ trajectories for the $n = 10$ and $n = 20$ materials derived from the 3-D analyses for both specimens. The response of the SE(B) and clamped SE(T) specimens with $a/W = 0.1$ and 0.2 is essentially similar as there is good agreement between the $J-Q$ trajectories for these configurations.

We now direct attention to the $J-Q$ trajectories for the clamped SE(T) specimens with $W/B = 0.5$ (see Fig. 3) displayed in Fig. 17; again, parameter Q is evaluated at the midplane location corresponding to $Z/(B/2) = 0$. As mentioned earlier, this crack configuration is recommended by DNV F-108 procedure [41] for experimental measurements of crack growth resistance curves of pipeline steels and their weldments using fracture specimens extracted from the longitudinal direction of the pipe. It can be seen that the $J-Q$ trajectories for the analyzed crack geometries displays only moderate sensitivity to specimen thickness as characterized by the W/B-ratio in comparison with the plots of Fig. 15. Here, a decreased W/B-ratio (increased specimen thickness) shifts the $J-Q$ curves slightly to the right, particularly for crack sizes corresponding to $a/W \geq 0.2$, indicating that this crack configuration exhibits a somewhat larger constraint loss at the same level of applied J than the specimen with $W/B = 1$. Overall, however, our analyses reveal that increasing specimen thickness relative to a fixed specimen width produces only small effects on the $J-Q$ trajectories and, consequently, on the expected fracture behavior of the specimen from $W/B = 1$ to $W/B = 0.5$.

5.3. 3-D results for circumferentially cracked pipes

We begin this section by first examining the variation of parameter Q with crack-tip distance. Fig. 18 (a–b) show Q-values computed at varying normalized distances $1 \leq r/(J/\sigma_0) \leq 5$, for the cracked pipes with $n = 10$ ($E/\sigma_0 = 500$) and $a/t = 0.2, 0.4$ at increased deformation levels. These Q-values are evaluated at the deepest point of the surface crack (see Fig. 6). The Q-values for the shallow crack ($a/t = 0.2$) and deep crack ($a/t = 0.4$) pipe are fairly

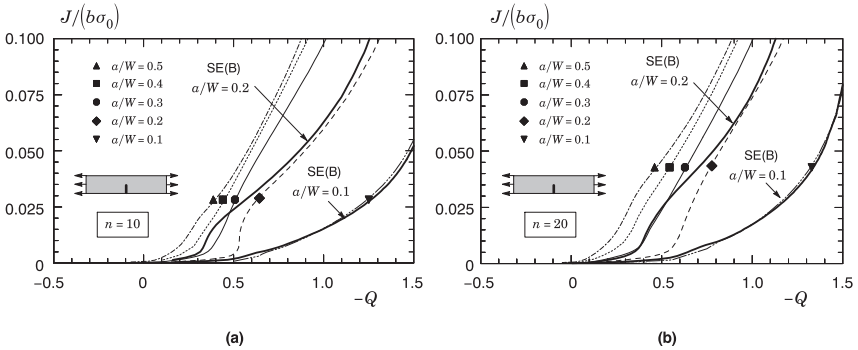

Fig. 16. Comparison of $J-Q$ trajectories at midplane specimen for the clamped SE(T) configuration with $W/B = 1$ and varying crack sizes and shallow notch SE(B) specimens with $W/B = 1$: (a) $n = 10$; (b) $n = 20$.

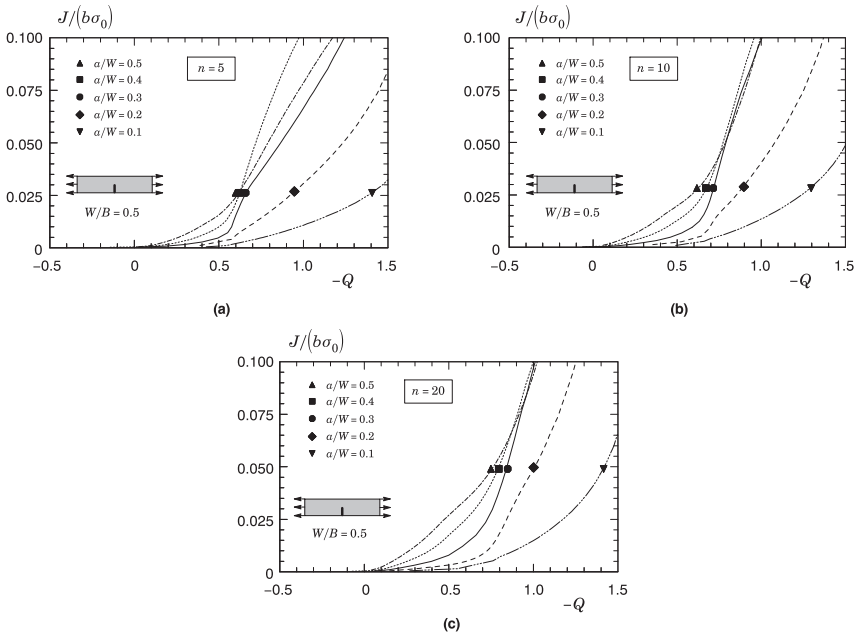

Fig. 17. $J-Q$ trajectories evaluated at midplane specimen for the clamped SE(T) configuration with $W/B = 0.5$ and different crack sizes and varying material properties: (a) $n = 5$ ($E/\sigma_0 = 800$); (b) $n = 10$ ($E/\sigma_0 = 500$); (c) $n = 20$ ($E/\sigma_0 = 300$).

independent of normalized distance, particularly at lower deformation levels. Fig. 18 also reveals that the Q-values for both pipe geometries consistently show slightly increased radial dependence under increasing loading, particularly for large applied J-values, which is nevertheless small in the range $1 \leq r/(J/\sigma_0) \leq 5$. Since the primary interest lies on assessments of fracture correlations between fracture specimens and a cracked pipe, the value of $r/(J/\sigma_0) = 2$ is also utilized to evaluate parameter Q for this crack configuration.

We now direct attention to the $J-Q$ trajectories for circumferentially cracked pipes subjected to reeling. Fig. 19 provides the evolution of parameter Q with increased values of J for the cracked pipe with varying crack sizes (as characterized by the a/t-ratio) and flow properties. Similar to the previous results, Q is defined by Eq. (4) at the normalized crack-tip distance given by $\bar{r} = 2$ and J is normalized by $b\sigma_0$ where b now denotes the remaining crack ligament $t-a$ (see Fig. 6). For all crack configurations and hardening materials, Q-values display a severe loss of constraint almost immediately upon loading. With increased deformation, Fig. 19(a) shows a somewhat large dependence of Q-values on a/t-ratio for the high hardening ($n = 5$) material. However, the $J-Q$ trajectories for the $n = 10$ and $n = 20$ materials with crack sizes in the range $0.2 \leq a/t \leq 0.4$ provided by Fig. 19(b–c) are nearly identical; here, only the trajectory for the shallow crack corresponding to $a/t = 0.1$ falls well below these curves.

The results displayed by the plots in Fig. 19(b–c) deserve attention because the materials with $n = 10$ and $n = 20$ typify hardening properties of high grade pipeline steels such as API X70 ~ X80 grade steels. The almost insignificant effect of crack size on the $J-Q$ trajectories for a/t-ratios larger that 0.2 may justify narrowing the choice of an appropriate crack size for the fracture specimen which adequately matches fracture behavior in a circumferentially cracked pipe. To make this point, Fig. 20 compares $J-Q$ trajectories for the cracked pipes with selected results for the SE(B) and clamped SE(T) specimens with the $n = 10$ material derived from the previous 3-D analyses. It can be seen that the $J-Q$ trajectories for the shallow notch SE(B) specimen with a/W between 0.1 and 0.2 encompasses entirely the corresponding evolution of crack front constraint for the cracked pipe. In contrast, the clamped SE(T) specimen maintains a somewhat higher level of

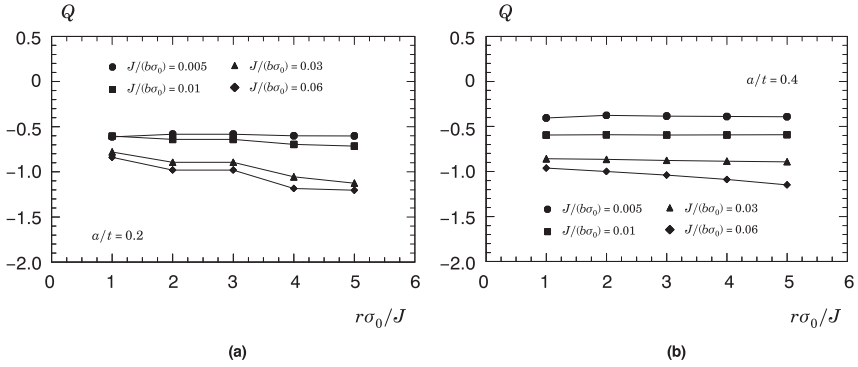

Fig. 18. Variation of parameter Q with normalized crack-tip distance for the circumferentially cracked pipe with $n = 10$ ($E/\sigma_0 = 500$) material: (a) $a/t = 0.2$; (b) $a/t = 0.4$.

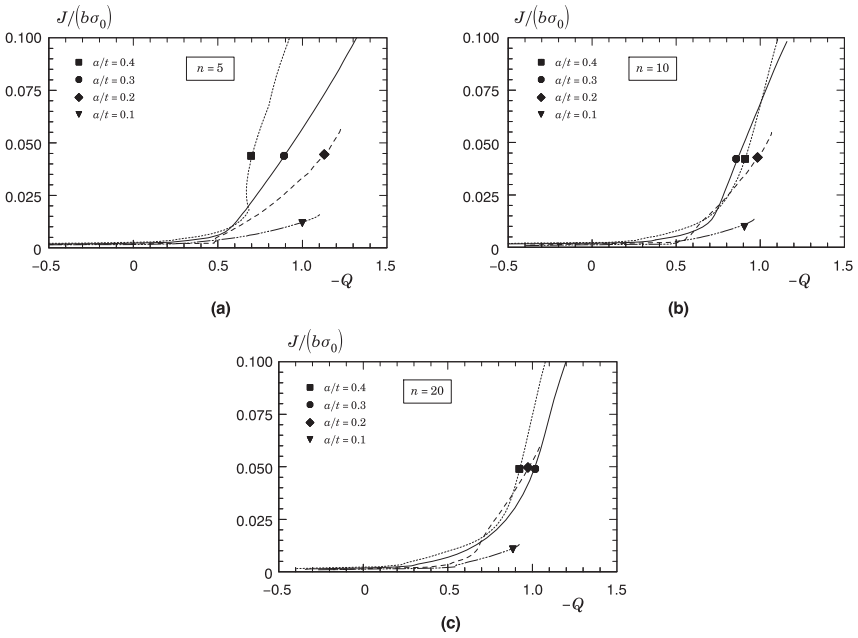

Fig. 19. J–Q trajectories evaluated at deepest point of the surface cracked for the pipe configuration with different crack sizes and varying material properties: (a) $n = 5$ ($E/\sigma_0 = 800$); (b) $n = 10$ ($E/\sigma_0 = 500$); (c) $n = 20$ ($E/\sigma_0 = 300$).

constraint compared to the J–Q curves for the cracked pipe. Although not shown here in interest of space, similar behavior is found for the n=5 and n=20 materials.

6. J–Q trajectories incorporating crack growth

The extensive numerical analyses of the SE(B) and clamped SE(T) fracture specimens, including the circumferentially cracked pipes, conducted thus far have not considered effects of ductile tearing on the evolving near-tip stress fields. Previous studies of Varias and Shih [39] and Dodds et al. [40] revealed varying crack-tip constraint for the growing crack relative to the stationary crack at the same level of applied J. Consequently, the previous J–Q trajectories for the fracture specimens and cracked pipes based on a stationary crack analysis may not reflect the potentially strong changes in the near-tip stresses due to increased crack growth.

Here, we address the effects of small amounts of crack growth, Δa, on the evolution of parameter $\widehat{Q}$ with increased remotely applied J for the analyzed crack configurations and implications for the correlation of fracture behavior between the fracture specimens and circumferentially cracked pipes. All the results presented in this section are for a typical API grade X70 pipeline steel tested by Hippert [43,49]; the flow properties and stress-strain response for this material were given previously in Section 4.4.

While the present study incorporating effects of crack growth on $J-\widehat{Q}$ trajectories is restricted to the pipeline grade steel employed in the ductile tearing analyses, it is nevertheless very representative of the crack growth behavior for a moderate hardening material – recall that the strain hardening exponent for this steel was estimated as $n = 13.3$ in Section 4.4. The large variety of possibilities associated with different combinations of strain hardening properties and initial porosity values, f_0, which reflects a diverse range of crack growth behavior for fixed material flow properties (for example, a low hardening material could exhibit a high or low tearing resistance depending on its microstructure and content of inclusion [24]), preclude extending these analyses to all hardening materials as in the case of the stationary crack analyses performed before. However, the broad features of the $J-\widehat{Q}$ trajectories incorporating crack growth computed here can be regarded as generic and the trends should apply to other hardening materials as well.

6.1. Calibration of cell parameters

Numerical simulation of ductile tearing in the fracture specimens and circumferentially cracked pipe described here begins with calibration of the cell parameters, f_0 and D, as outlined previously for the pipeline steel employed in this study. In all crack

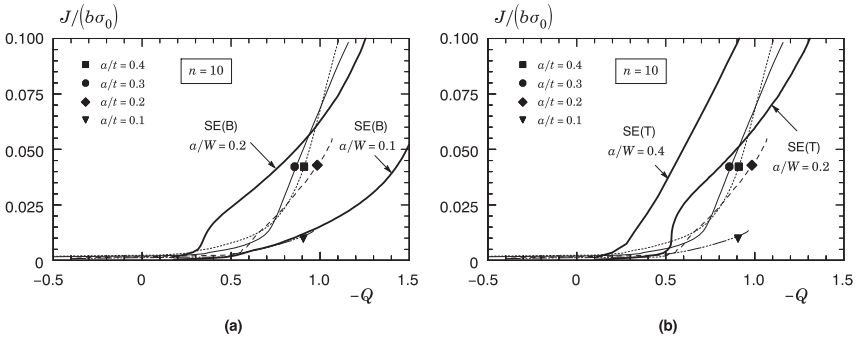

Fig. 20. Comparison of J–Q trajectories for the cracked pipes with selected results for the SE(B) and clamped SE(T) specimens with the $n = 10$ material.

growth analyses reported next, the cell extinction process using a linear-traction separation model described in Section 2 advances the crack when the current porosity, f, in the cell incident on the current crack tip reaches the critical value, $f_E = 0.15$. However, to improve the numerical response and to provide a more consistent description of the ductile tearing process, the location of the growing crack tip in the numerical analyses is taken at the cell with $f = 0.1$. Observe that this corresponds to a position between the cell currently undergoing extinction and the peak stress location; at this position stresses are decreasing rapidly and the void fraction is sharply increasing. Consequently, the use of slightly different f-values, other than 0.1, to define the crack-tip location for plotting purposes does not appreciably alter the R-curves (at a fixed J, the amount of crack extension would vary only by a fraction of the cell size) while, at the same time, smoothing the shape of the resulting crack growth resistance curve; Xia and Shih [21] and Ruggieri and Dodds [22] discuss this issue in detail.

The cell size D and initial porosity f_0 define the key parameters coupling the physical and computational models for ductile tearing. The measured resistance curve for a deeply cracked C(T) specimen ($a/W = 0.65$) tested by Hippert [43] (see also Hippert and Ruggieri [49]) using the unloading compliance technique is employed to calibrate these parameters. Within the present context, a series of finite element analyses is conducted to calibrate the cell parameters which establish agreement between the predicted J–Δa curve and experiments for a high constraint fracture specimen. Fig. 21 displays the measured crack growth resistance curve (average of two tests) in the TL orientation (described by the solid symbols in the plot) for the tested pipeline steel at room temperature. This fracture data was obtained using conventional 1-T C(T) specimens having the following dimensions: gross thickness, $B = 25$ mm, net thickness, $B_n = 20$ mm (20% side groove), width, $W = 50$ mm, $a = 32.5$ mm ($a/W = 0.65$). Hippert and Ruggieri [49] provide additional details of the material properties, including metallurgical characterization, and the fractures tests.

As described earlier in Section 4.3, we specify the cell size $D/2 = 100$ μm for the API X70 material employed in this study. While the cell parameters, D and f_0, control the cell response they should not be viewed as metallurgical parameters representing the microscopic observations of void spacing and initial void volume fraction but rather as computational parameters

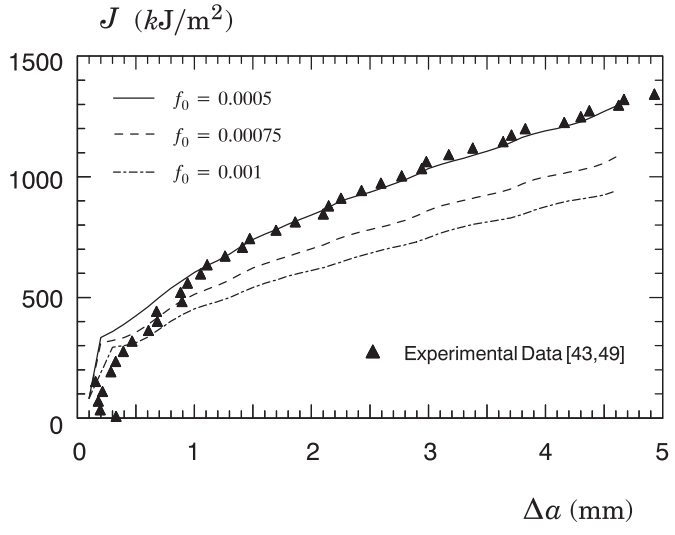

Fig. 21. Comparison of measured and predicted R-curve with different f_0-values for side-grooved 1-T C(T) specimen of API 5L-X70 at room temperature.

phenomenologically calibrated. Further, the calibrated values for D and f_0 clearly do not constitute a unique pair of parameters; for example, the numerical crack growth response of the fracture specimen scales almost proportionally with D for fixed value f_0 (a larger cell requires more total work to reach critical conditions). However, since D introduces an explicit length scale into the model thereby requiring the construction of a new mesh, it is obviously much less effort to fix D early on and then calibrate f_0.

Hence, with parameter D fixed, the calibration process then focuses on determining a suitable value for the initial volume fraction, f_0, that produces the best fit to the measured crack growth data for the deeply cracked C(T) specimen. Fig. 21 also shows the predicted J–Δa curves for this specimen. Predicted R-curves are shown for three values of the initial volume fraction, $f_0 = 0.0005$, 0.00075 and 0.001. For $f_0 = 0.0005$, the predicted R-curve agrees well with the measured values for almost the entire range of growth, albeit lying a little above the measured data for $\Delta a \leq 1$ mm in the blunting line region. In contrast, the use of f_0=0.001 produces a much lower resistance curve relative to the measured data. Consequently, the initial volume fraction $f_0 = 0.0005$ is thus taken as the calibrated value for the API 5L-X70 steel used subsequently in this study.

6.2. SE(B) and clamped SE(T) fracture specimens

Figs. 22 and 23 display the J–Δa curves and $J - \widehat{Q}$ trajectories (including ductile tearing) derived from the SE(B) and SE(T) growth analyses in 3-D with varying a/W-ratios which utilize the previous calibrated value of $f_0 = 0.0005$ for the X70 pipeline steel. For all sets of analyses, the computed resistance curves with crack extension and evolution of parameter $\widehat{Q}$ with crack-tip loading are defined at the centerplane ($Z = 0$ – see Fig. 5). To provide a comparison between the experimental measurements and predicted results, the open symbols in the plots of Figs. 22(a) and 23(a) indicate the measured R-curve with crack extension obtained by Hippert [43]; this crack growth data was employed to calibrate the cell parameter, f_0, utilized in these growth analyses for the SE(B) and SE(T) fracture specimens.

Consider first the computed crack growth resistance curves for both specimen geometries with varying a/W-ratios shown in Figs. 22(a) and 23(a). The resistance curves are essentially the same in the blunting line region ($\Delta a \lesssim 0.2$ mm) and then rise steadily with increased applied J. It can bee seen that the J–Δa curves for the SE(B) specimen displayed in Fig. 22(a) depend rather strongly on crack size for $a/W < 0.4$. Note that the crack growth behavior for the deeply-cracked configuration ($a/W = 0.5$) follows closely the measured R-curve for the tested high constraint C(T) specimen with $a/W = 0.6$ which thus provides strong justification for the adopted earlier calibration procedure of parameter f_0 based on a plane-strain growth analysis. Observe also in this plot the prominent influence of crack size (as characterized by the a/W-ratio) on the computed resistance curves for this crack configuration in the range $0.2 \leq a/W \leq 0.3$. A slightly different picture emerges for the computed fracture behavior of the clamped SE(T) specimen shown in Fig. 23(a). Here, the crack growth resistance curves exhibit relatively little sensitivity on the a/W-ratio. This plot shows that, for a fixed value of Δa, the fracture resistance in this specimen steadily increases by a moderate amount with decreased crack size. Very similar trends were also observed in the work of Nyhus et al. [50] who performed crack growth resistance tests using SE(T) specimens with varying a/W-ratios and found a weak dependence of measured R-curves on crack size.

Consider next the descriptions of crack-tip constraint in terms of $J - \widehat{Q}$ trajectories for the analyzed fracture specimens provided

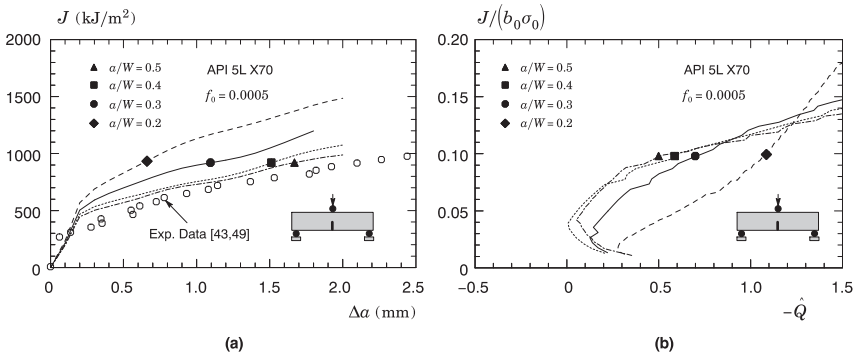

Fig. 22. 3-D growth analyses for the SE(B) fracture specimens with varying a/W-ratios: a) Computed J–Δa curves for $f_0 = 0.0005$; b) $J - \widehat{Q}$ trajectories for the extending crack.

in Figs. 22(b) and 23(b). Similar to the previous analyses, here $\widehat{Q}$ is defined by Eq. (5) at the normalized distance $\widehat{r} = 2$ whereas J is normalized by $b_0\sigma_0$ with b_0 denoting the remaining initial crack ligament defined by $W-a_0$ (again $J/(b_0\sigma_0)$ is plotted against $-\widehat{Q}$ to maintain positive scales) – here, we note that $\sigma_0 \equiv \sigma_{ys}$ in the present context. After a transitional stage at the early part of the curves for the SE(B) specimens with $a/W \geq 0.3$, in which there is a small increase in crack-tip constraint with parameter $\widehat{Q}$ varying from approximately −0.3 to −0.1, the evolution of $\widehat{Q}$ is essentially unchanged with increased values of J, particularly at higher deformation levels which correspond to larger amounts of ductile tearing. Observe, however, that the $J - \widehat{Q}$ trajectory for the shallow crack SE(B) specimen with $a/W = 0.2$ is shifted to the right compared to the other curves which clearly indicates lower levels of crack-tip constraint with increased applied J (and corresponding increased amounts of stable crack growth) for this crack configuration. This behavior is entirely consistent with the trends observed in the computed crack growth resistance curves shown in Fig. 22(a). Similar results are found for the $J - \widehat{Q}$ trajectories for the clamped SE(T) specimens displayed in Fig. 23(b). Here, all curves virtually merge onto one single curve which shows that the constraint levels with increased crack growth for this specimen are almost independent of crack size (as measured by the a/W-ratio).

6.3. Circumferentially cracked pipes

We now draw attention to the effects of crack growth on the fracture behavior for the 309 mm diameter ($D_e/t = 15$), circumferentially cracked pipe with varying crack depth ($a/t = 0.2$, 0.3, 0.4). Fig. 24 shows the crack growth resistance curves and $J - \widehat{Q}$ trajectories (including ductile tearing) derived from the growth analyses based upon the previous calibrated value of $f_0 = 0.0005$ for the X70 pipeline steel. For these analyses, the computed resistance curves with crack extension and evolution of parameter $\widehat{Q}$ with crack-tip loading are defined at the deepest point of the surface crack ($(Z = 0)$ – see Fig. 6). To facilitate comparisons with the computed fracture behavior derived from the previous analyses, these plots also include the corresponding results for key specimen geometries represented by the shallow crack SE(B) specimen with $a/W = 0.2$ and the deeply cracked SE(T) configuration with $a/W = 0.4$; this latter specimen is currently widely adopted in fracture tests to measure tearing resistance curves in terms of J–Δa for pipeline steels employed in advanced defect assessment procedures for submarine pipelines installed by the reeling process.

As clearly revealed in Fig. 24, the resistance curves and the $J - \widehat{Q}$ trajectories depend weakly on the a/t-ratio with a slightly more prominent effect in the range $0.2 \leq a/t \leq 0.3$. Observe the very high resistance curve associated with strongly negative $\widehat{Q}$-values for the circumferentially cracked pipe with $a/t = 0.2$. Now consider the J–Δa curves and $J - \widehat{Q}$ trajectories for the SE(B) specimen with $a/W = 0.2$ and the clamped SE(T) configuration with $a/W = 0.4$ displayed in these plots for the purpose of comparison. Remarkably, it is the shallow crack SE(B) specimen that behaves more similarly to the circumferentially cracked pipe than the clamped SE(T) configuration. The results in Fig. 24, taken together with the observed fracture response from the previous stationary crack analyses, provide compelling evidence that the shallow crack SE(B) specimen can accurately reproduce fracture resistance curves, albeit still slightly more conservative, in circumferentially cracked pipe under remote bend loading.

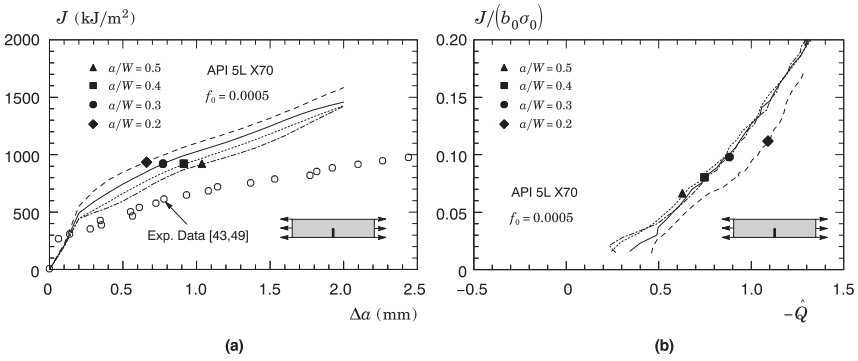

Fig. 23. 3-D growth analyses for the SE(T) fracture specimens with varying a/W-ratios: a) Computed J–Δa curves for $f_0 = 0.0005$; b) $J - \widehat{Q}$ trajectories for the extending crack.

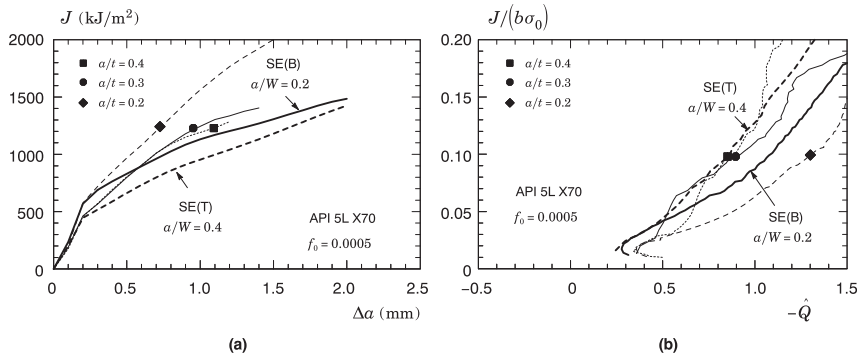

Fig. 24. 3-D growth analyses for the circumferentially cracked pipe with varying a/t-ratios: a) Computed $J-\Delta a$ curves for $f_0 = 0.0005$; b) $J - \widehat{Q}$ trajectories for the extending crack.

7. Summary and conclusions

This study describes a numerical investigation on the effects of crack front constraint in circumferentially surface cracked pipes subjected to bending load and conventional fracture specimens represented by clamped SE(T) and SE(B) geometries commonly employed to measure ductile tearing properties in pipeline grade steels. In the present work, attention is directed to cracked configurations, including the circumferentially cracked pipe with an external surface flaw, having varying crack sizes for different strain hardening materials. The methodology derives from a two-parameter description of crack-tip constraint in terms of $J-Q$ trajectories for stationary and growth analyses, supplemented by a micromechanics approach to model ductile tearing using computational cells, which are capable of including the potentially strong effects of ductile tearing on the evolving near-tip stress fields.

The extensive set of nonlinear finite element analyses for detailed plane-strain and 3-D models of fracture specimens and circumferentially cracked pipes conducted in this study show a rather complex interacting effect of specimen geometry, crack size and loading mode on the variation of crack front constraint with applied J. In particular, the growing analyses reveal features associated with the evolving near-tip stresses due to steady crack growth that would otherwise be neglected in conventional, stationary crack analyses. Overall, our numerical studies in connection with the adopted framework provide further insight and additional understanding in the correlation of fracture behavior for fracture specimens and cracked pipes based on a stress triaxiality parameter with important implications for current defect assessment procedures and specification of tolerable flaw sizes in girth welds of reeled pipelines.

The work described here supports the following conclusions and observations:

- Shallow crack bend specimens with crack sizes in the range $0.1 \leq a/W \leq 0.2$ exhibit levels of crack-tip constraint which are very similar to clamped SE(T) specimens having crack sizes in the range $0.2 \leq a/W \leq 0.4$. Hence, the measuring toughness capacity of the shallow crack bend configurations in terms of $J-\Delta a$ curves is comparable to the measuring capacity for fracture toughness of the clamped SE(T) specimens.
- The fracture behavior for the clamped SE(T) configuration displays little sensitivity on specimen thickness. The levels of crack-tip constraint for the $W/B = 1$ and $W/B = 0.5$ are similar thereby implying similar levels of measuring toughness capacity in terms of crack growth resistance curves.
- Crack growth resistance curves for the SE(B) specimens depend rather strongly on crack size, particularly for $a/W \leq 0.3 \sim 0.4$. In contrast, $J-\Delta a$ curves for clamped SE(T) specimens display little sensitivity on a/W-ratio.
- Shallow crack SE(B) specimens with crack sizes in the range $0.1 \leq a/W \leq 0.2$ provide fracture response described by $J-\Delta a$ curves in good agreement with the corresponding fracture behavior of circumferentially cracked pipes.

Since we have not explored other loading conditions, the trends and results obtained in this study are limited to the analyses of circumferentially surface cracked pipes subjected to remote bending. However, the new insights and understanding gained from this work encourages further investigations in direct correlations between laboratory fracture specimens and circumferentially cracked pipes for other loading scenarios such as, for example, subsea mechanically lined pipe installation by the reeling method with the application of internal pressure to prevent wrinkling and local buckling of the internal liner (see, *e.g.*, Focke [51]). Additional work is in progress to further validate the use of shallow-crack SE(B) specimens as an alternative fracture specimen to measure crack growth properties for pipeline steels and girth welds. Ongoing investigation also focuses on establishing robust correlations between J and CTOD for stationary and growing cracks in SE(T) and SE(B) fracture specimens.

Acknowledgments

This investigation is supported by Fundação de Amparo à Pesquisa do Estado de São Paulo (FAPESP) through Grants 2012/00094-2 and 2013/01139-2 provided to the first author (DFBS). The work of CR is also supported by by FAPESP through Grant 2012/13053-2 and by the Brazilian Council for Scientific and Technological Development (CNPq) through Grants 473975/2012-2 and 306193/2013-2. The authors acknowledge Petrobras for providing additional support for the work described here. The authors are also indebted to Dr. Eduardo Hippert Jr. (Petrobras) for providing the motivation to this work and for the many helpful and insightful discussions on ECA procedures for pipelines and submarine risers.

References

[1] Zerbst U, Ainsworth RA, Schwalbe K-H. Basic principles of analytical flaw assessment methods. Int J Press Vessel Pip 2000;77:855–67.
[2] Wiesner CS, Maddox SJ, Xu W, Webster GA, Burdekin FM, Andrews RM, et al. Engineering critical analyses to BS 7910-the UK guide on methods for assessing the acceptability of flaws in metallic structures. Int J Press Vessel Pip 2000;77:883–93.
[3] Anderson TL, Osage DA. API 579: a comprehensive fitness-for-service guide. Int J Press Vessel Pip 2000;77:953–63.
[4] British Energy Generation Limited. Assessment of the integrity of structures containing defects, R6 procedure; 2009.

[5] British Institution. Guide to methods for assessing the acceptability of flaws in metallic structures, BS 7910; 2013.
[6] American Petroleum Institute. Fitness-for-service. API RP-579–1 / ASME FFS-1; 2007.
[7] E. U. B.-E. Programme. Structural integrity assessment procedure, SINTAP; 1999.
[8] ASM International. ASM handbook – volume 11: failure analysis and prevention, vol. 12. Materials Park, OH: ASM International; 2002.
[9] Manouchehri S, Howard B, Denniel S. A discussion of the effect of the reeled installation process on pipeline limit states. In: 18th International Offshore and Polar Engineering Conference (ISOPE), Vancouver, Canada; 2008.
[10] Wästberg S, Pisarski H, Nyhus B. Guidelines for engineering critical assessments for pipeline installation methods introducing cyclic plastic strain. In: 23rd International Conference on Offshore Mechanics and Arctic Engineering (OMAE), Vancouver, Canada; 2004.
[11] Det Norske Veritas. Submarine pipeline systems. Offshore Standard OS-F101; 2010.
[12] Joyce JA, Hackett EM, Roe C. Effects of crack depth and mode loading on the *J-R* curve behavior of a high strength steel. In: Underwood JH, Schwalbe K-H, Dodds RH, editors. Constraint effects in fracture, ASTM STP 1171. Philadelphia: American Society for Testing and Materials; 1993. pp. 239–63.
[13] Joyce JA, Link RE. Effects of constraint on upper shelf fracture toughness. In: Reuter WG, Underwood JH, Newman J, editors. Fracture Mechanics, ASTM STP 1256. Philadelphia: American Society for Testing and Materials; 1995. pp. 142–77.
[14] Mathias LLS, Sarzosa DFB, Ruggieri C. Effects of specimen geometry and loading mode on crack growth resistance curves of a high-strength pipeline girth weld. Int J Press Vessel Pip 2013;111–112:106–19.
[15] Polanco MA, Nyhus B. Finite element procedures for constraint and limit load analyses for sent specimens and cracked pipes. Technical Report STF24, SINTEF Mater Chem Norway; 2001.
[16] Chiesa M, Nyhus B, Skallerud B, Thaulow C. Efficient fracture assessment of pipelines: a constraint-corrected SENT specimen approach. Eng Fract Mech 2001;68:527–47.
[17] Nyhus B, Polanco M, Ørjasæter O. SENT specimens as an alternative to SENB specimens for fracture mechanics testing of pipelines. In: 22nd International Conference on Ocean, Offshore and Arctic Engineering (OMAE), Vancouver, Canada; 2003.
[18] Xu J, Zhang ZL, Østby E, Nyhus B, Sun DB. Effects of crack depth and specimen size on ductile crack growth of SENT and SENB specimens for fracture mechanics evaluation of pipeline steels. Eng Fract Mech 2009;86:787–97.
[19] Xu J, Zhang ZL, Østby E, Nyhus B, Sun DB. Constraint effect on the ductile crack growth resistance of circumferentially cracked pipes. Eng Fract Mech 2010;77:671–84.
[20] Park DY, Tyson WR, Gianetto JA, Shen G, Eagleson RS. Evaluation of fracture toughness of X100 pipe steel using SE(B) and clamped SE(T) single specimens. In: 8th International Pipeline Conference (IPC), Calgary, Canada; 2010.
[21] Xia L, Shih CF. Ductile crack growth - I: a numerical study using computational cells with microstructurally-based length scales. J Mech Phys Solids 1995;43:223–59.
[22] Ruggieri C, Dodds RH. Numerical modeling of ductile crack growth using computational cell elements. Int J Fract 1996;82:67–95.
[23] Gullerud AS, Gao X, Dodds RH, Haj-Ali R. Simulation of ductile crack growth using computational cells: numerical aspects. Eng Fract Mech 2000;66:65–92.
[24] Garrison Jr WM, Moody NR. Ductile fracture. J Phys Chem Solids 1987;48:1035–74.
[25] Gurson AL. Continuum theory of ductile rupture by void nucleation and growth: part I – yield criteria and flow rules for porous ductile media. J Eng Mater Technol 1977;99:2–15.
[26] Tvergaard V. Material failure by void growth to coalescence. Adv Appl Mech 1990;27:83–151.
[27] Faleskog J, Shih C. Cell model for nonlinear fracture analysis – I: micro-mechanics calibration. Int J Fract 1998;89:355–73.
[28] Dodds RH, Shih C, Anderson T. Continuum and micro-mechanics treatment of constraint in fracture. Int J Fract 1993;64:101–33.
[29] Nevalainen M, Dodds RH. Numerical investigation of 3-D constraint effects on brittle fracture in SE(B) and C(T) specimens. Int J Fract 1995;74:131–61.
[30] Rice JR. A path independent integral and the approximate analysis of strain concentration by notches and cracks. J Appl Mech 1968;35:379–86.
[31] O'Dowd N, Shih C. Family of crack-tip fields characterized by a triaxiality parameter: part I – structure of fields. J Mech Phys Solids 1991;39:989–1015.
[32] O'Dowd N, Shih C. Family of crack-tip fields characterized by a triaxiality parameter: part II – fracture applications. J Mech Phys Solids 1992;40:939–63.
[33] J. R. Rice, Mechanics of crack tip deformation and extension by fatigue, in: J. Grosskreutz (Ed.), Fatigue crack propagation, ASTM STP 415, American Society for Testing and Materials, Philadelphia, 1967, pp. 247–311.
[34] Larsson SG, Carlsson AJ. Influence of non-singular stress terms and specimen geometry on small scale yielding at crack-tips in elastic-plastic materials. J Mech Phys Solids 1973;21:447–73.
[35] Betegon C, Hancock JW. Two-parameter characterization of elastic-plastic crack tip fields. J Appl Mech 1991;58:104–13.
[36] Du ZZ, Hancock JW. The effect of non-singular stresses on crack-tip constraint. J Mech Phys Solids 1991;39:555–67.
[37] Parks DM. Advances in characterization of elastic-plastic crack-tip fields. In: Argon AS, editor. Topics in fracture and fatigue. Springer Verlag; 1992. pp. 59–98.
[38] Cravero S, Ruggieri C. Correlation of fracture behavior in high pressure pipelines with axial flaws using constraint designed test specimens – part I: plane-strain analyses. Eng Fract Mech 2005;72:1344–60.
[39] Varias A, Shih CF. Quasi-static crack advance under a range of constraint steady-state fields based on a characteristic length. J Mech Phys Solids 1993;41:835–61.
[40] Dodds RH, Tang M, Anderson T. Numerical modeling of ductile tearing on cleavage fracture toughness. In: Kirk M, Bakker A, editors. Constraint effects in fracture: theory and application, ASTM STP 1244. Philadelphia: American Society for Testing and Materials; 1995. pp. 100–33.
[41] Det Norske Veritas. Fracture control for pipeline installation methods introducing cyclic plastic strain. DNV-RP-F108; 2006.
[42] Ruggieri C, Dotta F. Numerical modeling of ductile crack extension in high pressure pipelines with longitudinal flaws. Eng Struct 2011;33:1423–38.
[43] Hippert E. Experimental investigation of ductile fracture behavior in API X70 grade pipeline steels and applicability of crack growth resistance curves to predict the burst pressure in longitudinally cracked pipes. Ph.D. thesis. Polytechnic School, University of São Paulo; 2001 (In Portuguese).
[44] American Society for Testing and Materials. Standard test methods for tension testing of metallic materials. ASTM E8–11; 2011.
[45] Healy B, Gullerud A, Koppenhoefer K, Roy A, RoyChowdhury S, Petti J, et al. WARP3D: 3-D dynamic nonlinear fracture analyses of solids using parallel computers. Structural Research Series (SRS 607) UILU-ENG-95–2012. University of Illinois at Urbana-Champaign; 2013., http://code.google.com/p/warp3d.
[46] Anderson TL. Fracture mechanics: fundaments and applications. 3rd ed. Boca Raton, FL: CRC Press; 2005.
[47] Ruggieri C. FRACTUS2D: numerical computation of fracture mechanics parameters for 2-D cracked solids. Tech. rep. University of Sao Paulo; 2011.
[48] Silva LAL, Cravero S, Ruggieri C. Correlation of fracture behavior in high pressure pipelines with axial flaws using constraint designed test specimens – part II: 3-D effects on constraint. Eng Fract Mech 2006;76:2123–38.
[49] Hippert E, Ruggieri C. Experimental and numerical investigation of ductile crack extension in a high strength pipeline steel. In: ASME 2001 Pressure Vessels & Piping Conference (PVP 2001), Atlanta, GA; 2001.
[50] Nyhus B, Østby E, Knagenhjelm HO, Black S, Rostadsand PA. Experimental studies on the effect of crack depth and asymmetric geometries on the ductile tearing resistance. In: 24th International Conference on Ocean, Offshore and Arctic Engineering (OMAE), Vancouver, Canada; 2005.
[51] Focke ES. Reeling of tight fit pipe. Ph. D. Thesis. Technical University of Delft; 2007.